



저작자표시-비영리-변경금지 2.0 대한민국

이용자는 아래의 조건을 따르는 경우에 한하여 자유롭게

- 이 저작물을 복제, 배포, 전송, 전시, 공연 및 방송할 수 있습니다.

다음과 같은 조건을 따라야 합니다:



저작자표시. 귀하는 원저작자를 표시하여야 합니다.



비영리. 귀하는 이 저작물을 영리 목적으로 이용할 수 없습니다.



변경금지. 귀하는 이 저작물을 개작, 변형 또는 가공할 수 없습니다.

- 귀하는, 이 저작물의 재이용이나 배포의 경우, 이 저작물에 적용된 이용허락조건을 명확하게 나타내어야 합니다.
- 저작권자로부터 별도의 허가를 받으면 이러한 조건들은 적용되지 않습니다.

저작권법에 따른 이용자의 권리는 위의 내용에 의하여 영향을 받지 않습니다.

이것은 [이용허락규약\(Legal Code\)](#)을 이해하기 쉽게 요약한 것입니다.

[Disclaimer](#)

공학박사학위논문

**Numerical Simulation of Resin Flow and Mold Release
in UV Nanoimprint Lithography Process**

UV 나노임프린트 리소그래피 공정에서의
수지 유동과 이형 과정에 대한 수치해석

2014년 8월

서울대학교 대학원
기계항공공학부
손기주

**Numerical Simulation of Resin Flow and Mold Release
in UV Nanoimprint Lithography Process**

UV 나노임프린트 리소그래피 공정에서의
수지 유동과 이형 과정에 대한 수치해석

지도교수 이 우 일

이 논문을 공학박사 학위논문으로 제출함

2014 년 6 월

서울대학교 대학원

기계항공공학부

손 기 주

손기주의 공학박사 학위논문을 인준함

2014 년 6 월

위원장 : 최 만 수 (인)

부위원장 : 이 우 일 (인)

위 원 : 김 호 영 (인)

위 원 : 유 영 은 (인)

위 원 : 김 승 모 (인)



Numerical Simulation of Resin Flow and Mold Release in UV Nanoimprint Lithography Process

Kiju Sohn

School of Mechanical and Aerospace Engineering
Seoul National University

Abstract

Nanoimprint lithography (NIL) is a low-cost, high-throughput technique that is used to fabricate nano-scale patterns. In NIL, a resist material is deposited or dispensed on a substrate and a mold stamp presses the resist material to transfer precise patterns. NIL is usually classified into two categories depending on the resist material used. One is thermal NIL, which uses a thermoplastic material, and the other is UV NIL, which uses UV-curable resins. UV NIL uses a low-viscous UV resin which can be solidified quickly by a UV exposure. Therefore, compared to thermal NIL, UV NIL can produce higher resolutions with a shorter process time.

This study covers the resin flow and demolding characteristics of Step and Flash Imprint Lithography (SFIL), which is a conventional form of UV NIL. A numerical code was developed to analyze the behaviors of the liquid resin during the imprint process. The volume of fluid (VOF) method and the control volume finite element method (CVFEM) were used to demonstrate droplet spreading, merging, and void entrapment. A quantitative relationship between the resin volume and resin-spreading time was investigated for various dispensing recipes.

The characteristics of the resin which filled into feature cavities were also investigated by numerical analyses. The dissolution processes of gas pockets entrapped inside these feature cavities were investigated with a theoretical dissolution model. The effects of the feature geometry and process conditions on the feature-filling time were also studied.

The demolding process of SFIL was demonstrated by finite element analyses. The adhesion forces at the interface of the mold and imprinted pattern was expressed by a cohesive zone model. To verify the numerical models, experiments were conducted to measure the demolding forces while fabricating line and space patterns. The effects of the pattern geometry and cross-link shrinkage were studied in detail.

Using the numerical analysis techniques, several important issues pertaining to the SFIL process can be successfully analyzed. These analysis schemes can be applied to other UV NIL processes as well to optimize the process and reduce the production cost.

Keywords: Nanoimprint lithography (NIL), Resin flow, Capillary force, Gas void dissolution, Demolding, Volume of fluid (VOF) method, Cohesive zone model (CZM).

Student Number: 2010-30793

Table of contents

Chapter 1 Introduction	11
1.1. Overview	11
1.2. Research objective and scope	16
Chapter 2 Resin-spreading process	17
2.1. Research background	17
2.1. Analysis model	19
2.2. Code verification	24
2.3. Numerical result	25
3.4. Conclusion	30
Chapter 3 Feature-filling process	32
3.1. Research background	32
3.2. Analysis model	33
3.3. Numerical result	35
3.4. Conclusion	37
Chapter 4 Demolding process	39
4.1. Research background	39
4.2. Experiment	42

4.3. Analysis model.....	44
4.4. Numerical result.....	46
4.5 Conclusion.....	49
Summary	51
References	53
Figures	58
Tables	118

List of Figures

Figure 1 A typical photo lithography process	58
Figure 2 Nanoimprint lithography [3]: (a) a typical procedure of nanoimprint lithography (b) Si mold for a 70nm line pattern (c) 70nm PMMA line pattern imprinted with the Si mold	59
Figure 3 A three-dimensional pattern fabricated by the NIL process[4]	60
Figure 4 A typical procedure of step and flash imprint lithography (SFIL).....	61
Figure 5 Examples of commonly observed defects in UV NIL [13]	62
Figure 6 Removal of a residual layer and loss of feature dimension accuracy	63
Figure 7 An example of resin droplet spreading and gas void entrapment in SFIL.....	63
Figure 8 A schematic of liquid resin squeezed between the mold and substrate.....	64
Figure 9 Configuration and notations of control volume used in CVFEM.....	64
Figure 10 Concept of the volume of fluid (VOF) method	65
Figure 11 A flow chart for the gas void dissolution analysis	66
Figure 12 Imprio 100 S-FIL system (Molecular Imprints Inc., U.S.)	67
Figure 13 A quartz template used for Imprio 100 S-FIL system.....	67
Figure 14 Comparison of droplet diameters for various volumes after being pressed by an imprint force of 3N for 50 seconds	68
Figure 15 An analysis model of a gas void entrapped in the middle of a liquid resin film squeezed between two plates	69
Figure 16 Time evolution of the void diameter for various imprint pressures: comparison of (a) results from [22] and (b) results with the numerical code developed in this study	70
Figure 17 Droplet dispensing recipes: (a) single-drop, (b) spidergram, (c) repeated five drop, and (d) zigzag recipes	71
Figure 18 Examples of the resin-spreading simulation for three recipes: (a) single-drop,	

(b) spidergram, and (c) repeated five drop recipes	72
Figure 19 Time evolution of (a) the resin coverage rate and (b) resin film thickness with respect to the imprint force for the single-drop recipe.....	73
Figure 20 Time evolution of (a) the resin coverage rate and (b) resin film thickness with respect to the droplet volume for the single-drop recipe	74
Figure 21 Resin-spreading time of the single-drop recipe with respect to the droplet volume and imprint force.....	75
Figure 22 Time evolution of (a) the resin coverage rate and (b) resin film thickness with respect to the resin dispensing recipe	76
Figure 23 Resin-spreading time of the spidergram recipe for various droplet volumes and imprint forces	77
Figure 24 Resin-spreading time of the repeated five drop recipe for various droplet volumes and imprint forces.....	77
Figure 25 Comparison of resin-spreading times of the single-drop, spidergram and repeated five drop recipes	78
Figure 26 Analysis domain of the zigzag recipe	79
Figure 27 Entrapped gas dissolution simulation results: Gas concentration contours for different imprint forces	80
Figure 28 Time evolution of entrapped gas void diameters for imprint forces of 10N, 20N, and 40N.....	81
Figure 29 Time evolution of entrapped gas void pressure for imprint forces of 10N, 20N, and 40N.....	81
Figure 30 Entrapped gas dissolution simulation results: Gas concentration contours for different resin volumes	82
Figure 31 Time evolution of entrapped gas void diameters for total resin volumes of 25nl, 50nl, and 100nl	83
Figure 32 Time evolution of entrapped gas void pressure for total resin volumes of	

25nl, 50nl, and 100nl	83
Figure 33 Results of gas void entrapment tests with different residual layer thicknesses: (a) RLT=250nm, (b)RLT=500nm	84
Figure 34 Entrapped gas dissolution simulation results: Gas concentration contours for ambient gas pressures	85
Figure 35 Time evolution of entrapped gas void diameters for imprint pressures of 25.3kPa, 50.5kPa, and 101kPa.....	86
Figure 36 Time evolution of entrapped gas void pressure for imprint pressures of 25.3kPa, 50.5kPa, and 101kPa.....	86
Figure 37 Zigzag recipes with different droplet volumes and intervals.....	87
Figure 38 Time evolution of entrapped gas void diameters for dispensing intervals of 0.4mm, 0.6mm, and 0.8mm.....	88
Figure 39 Resin-spreading time with respect to the droplet interval	88
Figure 40 Comparison of resin-spreading times for various recipes	89
Figure 41 Time evolution of entrapped gas void diameters with respect to the diffusion coefficient	90
Figure 42 Resin-spreading time with respect to the diffusion coefficient.....	90
Figure 43 Example image of a non-fill defect [30].....	91
Figure 44 Relationship between the filling time and defect density of two types of patterns [30].....	91
Figure 45 Schematics of resin filling into pillar cavities during the SFIL process	92
Figure 46 Resin filling and gas dissolution model for pillar patterns	93
Figure 47 Time evolution of the feature-filling ratio into a pore with a 250nm radius and a 1000nm depth.....	94
Figure 48 Time evolution of the feature-filling ratio for pores with radii of 125nm, 250nm, 500nm, and 1000nm	95
Figure 49 Resin-filling time with respect to the pore radius.....	95

Figure 50 Time evolution of the feature-filling ratio for pores with depths of 250nm, 500nm, 1000nm, and 2000nm	96
Figure 51 Resin-filling time with respect to the pore height.....	96
Figure 52 Time evolution of the feature-filling ratio for imprint pressures of 12.5kPa, 25kPa, 50kPa, and 100kPa.....	97
Figure 53 Resin-filling time with respect to the imprint pressure.....	97
Figure 54 Time evolution of the feature-filling ratio for ambient pressures of 12.6kPa, 25.3kPa, 50.5kPa, and 101kPa.....	98
Figure 55 Resin-filling time with respect to the ambient gas pressure	98
Figure 56 Geometries of master molds and SEM images of the master mold cross- sections	99
Figure 57 Procedure of soft mold replication and imprint using the SFIL process	100
Figure 58 A quartz template: (a) before pattern replication and (b) after pattern replication	101
Figure 59 SEM images of cross-sections of imprinted patterns with (a) various heights and (b) various pitches.....	102
Figure 60 Demolding forces measured for various pattern heights	103
Figure 61 Demolding forces measured for various pattern pitches	103
Figure 62 Conceptual figure of the cohesive zone model.....	104
Figure 63 Cohesive zone model candidates.....	105
Figure 64 An example of finite element analysis model for demolding simulation. ..	106
Figure 65 An example of a demolding simulation result: stress contours.....	106
Figure 66 Comparison of experimental and numerical results with various cohesive zone models	107
Figure 67 A cohesive zone model chosen for the demolding analyses	107
Figure 68 Stress contours obtained by demolding simulations for various pattern heights: (a) $h_m = 250\text{nm}$, (b) $h_m = 500\text{nm}$, (c) $h_m = 750\text{nm}$, and (d)	

$h_m = 1000\text{nm}$	108
Figure 69 stress contours obtained by demolding simulations for various pattern itches: (a) $p_m = 1\mu\text{m}$, (b) $p_m = 2\mu\text{m}$, and (c) $p_m = 4\mu\text{m}$	108
Figure 70 Maximum demolding forces with respect to the pattern height	109
Figure 71 Maximum root stress with respect to the pattern height	109
Figure 72 Maximum demolding forces with respect to the pattern pitch	110
Figure 73 Maximum root stress with respect to the pattern pitch	110
Figure 74 Stress contours and deformed shapes of a line structure after volumetric shrinkages of 10% and 20%, respectively	111
Figure 75 Demolding simulation results with shrinkage rates of 0%, 10%, and 20%: (a) evolution of demolding forces and (b) maximum demolding forces	112
Figure 76 Maximum root stresses with respect to the shrinkage rate	113
Figure 77 Simulation model to investigate the shrinkage mismatch effect in the SFIL process	114
Figure 78 Effects of shrinkage mismatch in the SFIL process: simulation results with (a) RLT=50nm, (b) RLT=250nm, and (c) RLT=500nm	114
Figure 79 Stress contour and pattern deformation after 20nm mold shifting with a (a) soft mold and (b) hard mold	115
Figure 80 Maximum stress in the imprinted structure with respect to the mold eccentricity: Comparison when using a hard mold vs. a soft mold.	116
Figure 81 Demolding simulation results of partially filled line patterns with a filling ratio of (a)20%, (b)40%, (c)60%, (d)80%, and (e)100%	117
Figure 82 Demolding forces of partially filled line patterns	117

List of Tables

Table 1 Material properties and process conditions used for the single-drop spreading simulation	118
Table 2 Physical parameters used for the gas dissolution simulation	119
Table 3 Process parameters used for the feature-filling analysis	120

Chapter 1 Introduction

1.1. Overview

Currently, micro/nano-structures are widely used in various engineering and scientific fields. Precise patterns are used for cutting-edge devices such as high-resolution displays, smart-phones, tablet PCs, information storage devices, biochips, and optical instruments. Over the last 20 years, numerous technologies have been developed to fabricate micro/nano-structures, including photolithography, scanning beam lithography, microcontact printing, and imprint lithography [1]. Among them, photo lithography is most commonly used in the industry (see Figure 1). The photo lithography process has the advantages of reproducibility and high yield ratios as well as high resolutions. However, photo lithography requires expensive optical equipment, which increases the production cost tremendously [2]. Moreover, photolithography is not feasible for the fabrication of large-area patterns owing to its limitation related to the intensification of light sources onto a large area and the distortion of optical images.

To overcome the drawbacks of the conventional techniques, Chou et al. [3] proposed a novel lithography technique termed nanoimprint lithography (NIL) in 1996. NIL was introduced as a promising technique fabricating low-cost micro/nanometer-scale patterns with a high throughput and high resolution. For NIL, a resist material is

introduced onto a substrate and pressed by a mold stamp, after which the nano-structures on the mold stamp surface are transferred to the resist film. After the solidification of the resist material, the resist film and mold stamp are separated. The imprint process is followed by an etching process, such as reactive ion etching (RIE), which is used to remove the residual resist in the imprinted area(see Figure 2) [3]. Given that NIL is based on direct mechanical contact between the mold and resist material, one of the most prominent advantages of NIL is its ability to produce three-dimensional patterns at one time. Figure 3 shows an example of three-dimensional patterns imprinted by NIL [4].

Since NIL was first introduced in 1996, there have been efforts to improve this novel idea. In 1997, the Chou's research group successfully fabricated arrays of holes with a diameter of 10nm and a period of 40nm by NIL [5]. To overcome the problems of a high imprint pressure and high-temperature process conditions in the earliest forms of NIL processes, Willson's research group at the University of Texas at Austin suggested a different technique, which they termed Step and Flash Imprint Lithography (SFIL) in 1999, during which they used a low viscosity, photopolymerizable, organosilicon solution as a resist material. Features smaller than 60nm in size have been reliably produced using this imprinting process [6]. Willson's research group also demonstrated in 2002 polymer-on-Si semi-dense lines of less than 50 nm made with the SFIL process [7]

Chou's research group also introduced two types of roller imprint lithography processes (RIL) [8]. Using these techniques, they were able to achieve a sub-100nm resolution. However, the procedure was just feasible for a small piece of Si mold onto a Si substrate.

Ahn and Guo developed a continuous roll-to-roll imprint lithography (R2RIL) process on a flexible plastic substrate in 2008 [9]. They tried two types of liquid resist materials for the R2RIL application. One was a quick, thermal-curable liquid resist based on a modified form of PDMS, and the other was UV-curable low-viscosity epoxysilicone. They successfully produced a PDMS grating pattern with a period of 700nm period and a width of 300nm imprinted on a PET strip with thermal R2RIL, and an epoxysilicone pattern with a period of 100nm and a width of 70nm with UV R2RIL. Ahn and Guo also demonstrated large-area (4in wide) continuous imprinting of nanogratings using both R2RIL on a flexible web and roll-to-plate imprint lithography(R2PIL) on a rigid substrate [10]. Grating patterns with a 300nm linewidth were continuously transferred on a glass substrate in the R2PIL mode.

NIL is usually classified into two categories, thermal NIL and UV NIL, depending on the resist materials used. Thermoplastic polymers are used as a resist material in the thermal NIL, while UV-curable monomer solutions are generally used for UV-NIL. Comparing the two techniques, UV-NIL is preferred to the thermal NIL, as it is much easier to achieve high-resolution patterns with UV NIL because UV NIL uses less

viscous UV-curable resins instead of highly viscous thermoplastic polymers. In addition, the UV NIL requires a low imprint pressure, while the thermal NIL process involves a high imprinting pressure which can damage the substrates or pre-existing structures. Moreover, thermal NIL requires heating and cooling cycles, which increase the process time significantly. In UV NIL, the resin is cured in a very short time when it is exposed to UV rays [11]. Therefore, UV NIL is more appropriate for the mass production of precise patterns than thermal NIL.

This study covers Step and Flash Imprint Lithography (SFIL), the basic form of the UV NIL process introduced by Wilson's research group in 2005 [6]. In SFIL, a low viscosity, photopolymerizable monomer resin is introduced onto a transfer layer coated on a substrate. It is then pressed by a hard, flat and transparent stamp with nano-structures on the surface. After the imprinting process is completed, UV rays cure the photopolymer, leaving a solidified replica of the template. The mold template and imprinted polymer pattern are then separated [6, 7, 12]. Figure 4 illustrates the typical SFIL procedure.

SFIL is a promising technology for the mass production of large-area nano-structures. However, SFIL has important issues to overcome. Among these issues, defect control is one of the main technical challenges. The most common defects in SFIL are shown in Figure 5 [13]. These defects can affect not only the field in which they occur, but also all subsequent fields.

The line break and non-fill defects are typically induced by gas void entrapment. When the resin droplets are squeezed between the substrate and mold stamp, they spread and merge with adjacent droplets. During the merging process, ambient gas can be entrapped inside the liquid resist. Even one small gas bubble remaining can cause a serious defect. Therefore, it is important to control both gas ventilation and the dissolution of entrapped gas voids. However, it is not easy to predict how large the gas bubbles will form initially and how long it will take for the entrapped gas to be dissolved completely. Moreover, it is also challenging to detect or observe droplet behavior and gas bubble formation, as both phenomena occur too quickly and because the size of the entrapped bubbles are usually too small. Therefore, a numerical simulation can serve to predict resin behavior and gas bubble formation during the UV NIL process.

Another problem that arises is contamination of the mold surface. Once mold contamination takes place, the contamination remains for good, causing repeated defects on the imprinted patterns. One of the main causes of mold surface contamination is pattern fractures or rip-off failures during the demolding process. The adhesion force between the imprinted pattern and mold is the main cause of the demolding failure [14, 15]. Therefore, the demolding process should also be considered as important as the imprint process itself in SFIL.

1.2. Research objective and scope

The objective of this study is to improve imprint quality and productivity of SFIL by evaluating its process conditions. To achieve this objective, techniques to predict the results of SFIL sub-processes are required. In this study, numerical analysis schemes were developed to cover the complete processes of resin-spreading, gas void entrapment, gas void dissolution, and mold releasing.

Various resin-dispensing recipes were evaluated by a numerical analysis code developed in this study. The research focused especially on a reduction of both the resin-spreading time and the residual layer thickness.

The characteristics of resin filling into the pillar feature cavities were also investigated by numerical analysis models. Capillary effects and the dissolution of the entrapped gas were considered together.

Finally, the demolding processes of SFIL were investigated by finite element analyses using a cohesive zone model. To verify the analyses models, demolding forces were measured while fabricating line and space patterns using SFIL. Based on the experimental results, appropriate finite element models were proposed to demonstrate the demolding process. The effects of the pattern geometry, pattern shrinkage rate, mold shift, and filling ratio on the SFIL demolding process were investigated in detail.

Chapter 2 Resin-spreading process

2.1. Research background

In SFIL, UV-curable liquid resin is introduced onto the surface of a substrate. The resin is then pressed by a mold stamp and spread to cover the imprint area. At the point, how fast the resin spreads is an important issue in terms of reducing the process time. Therefore, predicting the resin-spreading time for a given resin-dispensing recipe is crucial in a design of a SFIL process.

Colburn et al. [16] analyzed the fluid behavior between a substrate and a mold based on lubrication theory [17]. They also considered the effects of the capillary force and fluid viscosity. Their results showed that imprint pressure increases drastically to maintain a constant mold velocity as the residual layer thickness decreases. It was also concluded that, when it comes to a reduction of the resin-spreading time, applying multiple droplets is a better option than a single-droplet approach. Raddy et al. [18] presented a simulation model of the flow and coalescence of the multiple fluid drops. They also used lubrication theory to simplify the fluid behavior and solved a two-dimensional fluid dynamics problem. The volume of fluid (VOF) method [19] was used to define the fluid interface and thus track the fluid movement accurately.

Another issue with regard to SFIL is to reduce the residual layer thickness. The

formation of a residual layer during the imprinting process is inevitable. However, minimization of the residual layer thickness is of great importance because the layer has to be removed by a plasma etching process prior to the pattern transfer onto a substrate. The plasma etching process results in a loss of dimensional accuracy and has to be minimized (see Figure 6). Schmitt et al. [20] studied the dependence of the residual layer thickness on the viscosity and the initial dispensed volume. They theoretically predicted that the residual layer thickness increases with the square root of the viscosity of the resist. Kim et al. [21] developed a zigzag type of dispensing recipe to pursue a thin and uniform residual layer thickness. The optimized dispensing recipe yielded a much thinner residual layer than a conventional spidergram-type recipe. Moreover, the zigzag recipe improved the uniformity of the residual layer thickness as well.

When the droplets are being compressed and spread around, adjacent droplets merge, resulting in gas void entrapment among the droplets. The gas voids should be dissolved into the resin during the imprint process. However, they sometimes remain undissolved, resulting in serious pattern defects. Figure 7 shows an example of the resin droplet spreading and gas void entrapment in SFIL.

Liang et al. [22] studied the air bubble formation and dissolution phenomena of SFIL. They investigated the effects of the initial size of the air bubble, the imprinting pressure, the air solubility, and the resist residual layer thickness on the air bubble

dissolution time. They concluded the air in a bubble can be completely dissolved in a resist liquid as long as the bubble is smaller than a critical size. Usuki et al. [23] also observed the process of resist spreading and air bubble dissolution. They showed that smaller resist droplets with a higher dispensing density could reduce the bubble dissolution time.

In this chapter, various droplet dispensing recipes were evaluated by numerical simulations. The resin-spreading, gas void entrapment, and gas dissolution processes were analyzed with the control volume finite element method (CVFEM) [24]. To define the resin area and gas area, the volume of fluid (VOF) method [19] was also used for the analyses.

2.1. Analysis model

A numerical analysis code was developed for the droplet spreading and gas dissolution simulations. Figure 8 illustrates the cross-section of a mold and substrate which are pressing liquid resist between them. Here, h_R is the gap between the mold and substrate, or the residual layer thickness. As the gap between the mold template and substrate is very thin compared to the in-plane dimensions of the imprint area, the flow was assumed to be a Hele-Shaw flow [25]. The mass conservation equation for this system can be expressed as follows:

$$\frac{\partial \bar{u}}{\partial x} + \frac{\partial \bar{v}}{\partial y} = -\frac{\dot{h}_R}{h_R} \quad (2.1)$$

Here, x, y, \bar{u}, \bar{v} , and \dot{h}_R are the two inplane coordinates, the two average resist velocities in the x and y directions, and the mold velocity in the z direction, respectively.

Assuming that the fluid is a generalized Newtonian fluid and that the velocity profile in the z direction has a parabolic shape with a no-slip condition at the wall (see Figure 8), the relationship between the fluid pressure and average velocities \bar{u} and \bar{v} can be expressed as [25]

$$\bar{u} = -\frac{S}{h_R} \frac{\partial p}{\partial x} \quad (2.2.a)$$

$$\bar{v} = -\frac{S}{h_R} \frac{\partial p}{\partial y} \quad (2.2.b)$$

where S is the flow conductance, which is defined as $h^3/12\mu$, while p and μ are the average pressure and viscosity of the resist material, respectively. Substituting equations (2.2a) and (2.2b) into equation (2.1), the governing equation can be obtained as follows:

$$\nabla \cdot \left(\frac{S}{h_R} \nabla p \right) = \frac{\dot{h}_R}{h_R} \quad (2.3)$$

Equation (2.3) was discretized by the control volume finite element method(CVFEM) [24]. Figure 9 depicts the configuration and notations of the control volume used in the CVFEM. Considering a control volume associated with node “ i ” in Figure 9, the following equation can be derived from equation (2.3) by applying the divergence theorem [24].

$$\sum \left[\int_a^o \frac{S}{h_R} \nabla p \cdot \hat{n} dS + \int_o^c \frac{S}{h_R} \nabla p \cdot \hat{n} dS - \int_{iaoc} \frac{\dot{h}}{h_R} \right] + \text{boundary conditions} = 0 \quad (2.4)$$

Assuming the pressure field in an element as

$$p(x, y) = Ax + By + C, \quad (2.5)$$

where A , B , and C are constant pressure coefficients, equation (2.4) can be discretized into the form of

$$[D_{ij}] \{p_j\} = -\{E_i\} \quad (i, j = 1, 2, \dots, N), \quad (2.6)$$

where $[D_{ij}]$, $\{p_j\}$, $\{E_i\}$, and N are the flow conductance matrix, pressure field vector, vertical flow rate vector, and total number of nodes, respectively.

After obtaining the pressure field by solving equation (2.6), a velocity field was

obtained with equations (2.2.a.) and (2.2.b). From the calculated velocity field, the inflow and outflow of the fluid fraction in each control volume was calculated. Then, the flow front (or interface between the liquid and gas) was defined by the VOF method [19]. Figure 10 depicts the concept of the fluid fraction in VOF. If a control volume is completely charged with the liquid, the fluid fraction of the control volume has a value of unity ($f = 1$). Meanwhile, the fluid fraction of the empty control volume is zero ($f = 0$). If a control volume is partially charged, the fluid fraction has a value between 0 and 1 ($0 < f < 1$). The location of the flow front is defined as a point where the fluid fraction has a value of 0.5 ($f = 0.5$).

The boundary condition was given as a pressure set. At the boundary of the droplet, the pressure was given as a summation of the ambient pressure and the pressure induced by capillary forces. Using the Young-Laplace equation [26], the boundary condition at the flow front was applied as:

$$P_{boundary} = P_{amb} - \frac{\gamma(\cos \theta_1 + \cos \theta_2)}{h_R} \quad (2.7)$$

where P_{amb} , γ , θ_1 , and θ_2 are the ambient pressure, surface tension of the resist, and contact angle with the mold and the substrate, respectively.

When a gas bubble is entrapped, the bubble is compressed dissolving into the liquid

resist. In the bubble dissolution analysis, the main assumption was that the gas bubble was compressed until it reached the equilibrium gas void pressure “ p_v ”, which is given as [26]

$$p_v = p_{imp} + \gamma \left(\frac{(\cos \theta_1 + \cos \theta_2)}{h_R} + \frac{1}{R_v} \right) \quad (2.8)$$

where P_{imp} and R_v are the imprint pressure and the radius of the gas void, respectively. As the gas in the void dissolves into the resist, the volume of the void becomes smaller to maintain its equilibrium pressure.

In the gas dissolution process, the time rate of change of the gas concentration in the resist can be described by the following equation:

$$\frac{\partial n}{\partial t} = D \nabla^2 n - \nabla \cdot (n \vec{v}) \quad (2.9)$$

Here n , D and \vec{v} are the gas concentration, the diffusion coefficient and the velocity vector of the fluid, respectively. The boundary condition for the gas dissolution process is given as

$$n_v = C_h P_v, \quad (2.10)$$

where n_v and C_h are the gas concentration at the void boundary and Henry's

constant, respectively. Equation (2.9) associated with the gas dissolution process was solved explicitly. Figure 11 illustrates a flow chart of the gas dissolution analysis algorithm.

2.2. Code verification

In order to verify the numerical code developed in this work, two types of numerical analyses have been conducted. One was a single-drop spreading analysis and the other was a bubble dissolution analysis.

For the single-drop spreading test, an Imprio 100 S-FIL system (Molecular Imprints Inc., USA) was used. Droplets with different volumes are dispensed on a Si substrate and pressed by a flat quartz stamp with 3N per drop for 50 seconds. Figure 12 shows the Imprio100 S-FIL system and Figure 13 is an image of the quartz stamp. Numerical simulations were conducted with the same test conditions. The material properties and process conditions used for the simulation are given in Table 1. Figure 14 compares the experimental and numerical results, which show good agreement.

In order to verify the gas dissolution analysis code, the same test conducted in an early study [22] was conducted here as well. Figure 15 depicts the finite element model used for the code verification. A gas bubble entrapped in the middle of a liquid film is dissolved until it disappears. The initial bubble diameter, the liquid film diameter, and

the liquid film thickness were 180 μm , 20mm, and 25nm, respectively. The liquid film was pressed by various imprint pressures. The physical properties used for the dissolution simulation are given in Table 2. The results of the reference and those with the numerical code developed in this work showed good agreement as presented in Figure 16.

2.3. Numerical result

Using the numerical analysis code developed here, four different resin-dispensing recipes were evaluated in terms of both resin-spreading time and the residual layer thickness. Schematics of four recipes, which are termed as the single-drop recipe, spidergram recipe, repeated five drop recipe, and zigzag recipe, are given in Figure 17. The spidergram recipe is a pre-programmed recipe used in the Imprio100 S-FIL System. The repeated five drop recipe was devised by Lee's research group [27] and the zigzag recipe was proposed by Kim et al. [21].

The imprint area was designed as a 20mm by 20mm square. The material properties and process conditions are identical to those given in Table 1 unless otherwise noted. Figure 18 shows examples of resin-spreading analyses results of the first three recipes. The total volume of the resin was 100nl and the imprint force was 40N. The gas does not get entrapped inside the resin for the three recipes, as shown in Figure 18.

Figures 19 and 20 depict the simulation results of the single-drop recipe. Resin drops of 100nl, 200nl, 400nl, and 800nl were pressed by imprint forces of 10N, 20N, and 40N, respectively. Figures 19 (a) and (b) are the results with respect to the imprint force. The results show that as the imprint force increases, the resin-spreading time decreases. Meanwhile, Figures 20 (a) and (b) are the results with respect to the resin volume. The figures show that a decrease in the resin volume increases the resin-spreading time. Moreover, the resin spreads rapidly at the beginning of the mold pressing process, but the spreading speed becomes slower as the resin continues to spread, as a thinner residual layer results in greater fluid resistance. Figure 21 shows the relationship between the droplet volume and the resin-spreading time with respect to different imprint forces. As shown in Figure 21, the time required for the resin to cover the imprint area increases drastically as the resin volume becomes smaller (i.e., the residual layer becomes thinner).

Figure 22 compares the simulation results of the single-drop, spidergram, and repeated five drop recipes. Resin drops with a total volume of 100nl were pressed by an imprint force of 40N. Figures 22(a) and (b) depict the time evolution of the rate of resin coverage and the resin film thickness, respectively. Figures 23 and 24 present resin-spreading time for the spidergram and repeated five drop recipes, respectively. The results of both the spidergram and repeated five drop recipes are similar to that of the single-drop recipe. That is, as the resin volume decreases, the resin-spreading time

increases, while the increase of the imprint force reduces the resin-spreading time.

The results of the three recipes are combined in Figure 25. With the spidergram and repeated five drop recipes, the resin-spreading time decreased significantly compared to the single-drop recipe. However, the two recipes also showed limitations when used to imprint patterns with a very thin residual layer.

The zigzag recipe was evaluated by numerical analyses as well. As shown in Figure 26, a triangular analysis domain was considered to reduce the computation time. A symmetric boundary condition was given at the boundary of the analysis domain to demonstrate repeated droplet arrays. Henry's law constant, used for the analyses, was adopted from earlier work [22] as $C_h = 5.45 \times 10^{-5} \text{ mol} \cdot \text{m}^{-3} \cdot \text{Pa}^{-1}$. Meanwhile, the diffusion coefficient was estimated by the Stokes-Einstein equation as $D = 2.84 \times 10^{-10} \text{ m}^2 \cdot \text{s}^{-1}$, considering an effective diameter of the nitrogen molecule of 0.304nm [28].

First, the void dissolution process for the zigzag recipe with respect to the imprint pressure was studied. Resin droplets with a total volume of 100nl were dispensed on a 20mm by 20mm square imprint area in 400 μm intervals. Then, they were pressed by imprint forces of 10N, 20N, and 40N, respectively. Figure 27 shows contours of gas concentration dissolved in the resin. Figures 28 and 29 present the time evolution of entrapped gas void diameters and the gas void pressure, respectively. The results show

that a higher imprint pressure increases the pressure inside the gas void, resulting in better gas solubility of the resin.

Second, the effects of the residual layer thickness on the gas void solubility were investigated. The droplets were also dispensed with a 400nm interval and pressed by a 10N imprint force. The results with total resin volumes of 25nl, 50nl, and 100nl are given in Figures 30, 31, and 32. When the droplet intervals are the same, an increase in the droplet volume decreases entrapped gas dissolution time, as the gas pressure inside the void decreases. This occurs because the capillary pressure decreases as the gap between the mold and substrate increases for a larger resin volume. Figure 33 shows an experimental result which determined if the size of the gas void becomes smaller when the residual layer is thinner. Here, nine resin drops are dispensed on a 20mm by 20mm imprint domain to form four gas voids after being pressed by a flat quartz stamp. Comparing the images in Figure 33, the case with a total resin volume of 200nl(RLT=500nm) forms a larger gas void than the 100nl(RLT=250nm) case. Therefore, the numerical results are proved to be reasonable.

Third, the effects of ambient gas reduction were investigated. Droplets with a total volume of 100nl were dispensed at 400nm intervals and pressed by an imprint force of 10N. The ambient gas was considered to be 25.3kPa, 50.5kPa, and 101kPa, in three cases. From the results given in Figures 34~36, a reduction of the ambient gas pressure can decrease the dissolution time of the entrapped gas void effectively. However, a

reduction of the ambient gas can lead to resin evaporation, as UV-curable resins are extremely volatile.

Last, the effects of the droplet interval were studied. A total resin volume of 100nl was dispensed with different droplet intervals of 0.4mm, 0.6mm, and 0.8mm (see Figure 37). This makes the volume of one droplet for each case 34.6pl, 77.9pl, and 138.4pl, respectively. As shown in Figures 38 and 39, the longer the dispensing interval becomes, the more time the gas void takes to dissolve, as the initial size of the entrapped gas void is larger for the longer dispensing interval. Therefore, to reduce the gas void dissolution time, resin droplets with a small volume should be dispensed densely. However, when a droplet volume becomes smaller, the rate of evaporation also increases[21]. That is, smaller droplets take much less time to evaporate than larger droplets. Therefore, small droplets should be dispensed by multiple nozzles to reduce the dispensing time and keep the previously dispensed droplets from evaporating.

The results of the four recipes are compared in Figure 40. When patterns are imprinted on a 20mm by 20mm square imprint domain, the spidergram and repeated five drop recipes are efficient for residual layers thicker than 100nl (RLT=250nm). However, the zigzag recipe is a better option for resin volumes less than 100nl.

In this study, the diffusion coefficient of ambient gas into the UV-curable liquid resin

was obtained by the Stokes-Einstein relationship, which was originally derived to describe the diffusion motion of a Brownian particle in a solvent of much smaller particles. Therefore, the Stokes-Einstein relationship works very well for describing the diffusion of a macroscopic body in a solvent. However, the monomers in the UV-curable resins are usually larger than ambient gas molecules. Therefore, an experimental measurement of the diffusion coefficient is recommended for more accurate analysis results.

The effects of the diffusion coefficient of the gas dissolution time for the zigzag recipe were investigated. As shown in Figures 41 and 42, as the diffusion coefficient decreases, the entrapped gas dissolution time increases drastically.

3.4. Conclusion

Resin-spreading characteristics of SFIL were investigated by numerical analyses. Four different dispensing recipes were compared in terms of the resin-spreading time. The spidergram and repeated five drop recipes showed much shorter resin-spreading time compared to the single-drop recipe. However, as the residual layer thickness becomes thinner, the resin-spreading time of the spidergram and repeated five drop recipes increased drastically. Meanwhile, the zigzag recipe is not limited by the residual layer thickness, although gas void entrapment is inevitable for the recipe. In

order to reduce the gas void dissolution time, smaller resin droplets should be dispensed in shorter intervals.

Chapter 3 Feature-filling process

3.1. Research background

In SFIL, it is essential to fill the feature cavities with the resist completely to replicate the features with better accuracy. Incomplete filling of the feature cavity could potentially affect the yield and quality of the transferred patterns. Therefore, it is necessary to understand and quantify the characteristics of the feature-filling phenomena in SFIL.

In general, it is known that the pattern features are filled with a low-viscous liquid resist by capillary actions in SFIL [29]. Thus, a longer filling time is required for large pattern features [30]. Figure 43 is an example image of a non-fill defect, and Figure 44 shows the relationship between the filling time and the defect density of small and large patterns.

Chauhan et al. [29] analyzed the feature-filling phenomena for SFIL via the diffusion of a gas, entrapped in the features, through a liquid imprint resist. They investigated the gas concentration profile across the liquid resist drop, the filling progression, and the total filling time for different pattern configurations. Yoneda et al. [30] also analyzed the SFIL filling process by means of a fluid simulation. They used a free-surface flow model with a finite volume method. Hirai [31] solved the Navier-

Stokes equation numerically for a resist flow into a pattern. He presented bubble-trapping characteristics for various contact angles with the template and the substrate.

The feature-filling process in SFIL is analyzed numerically in this chapter. The capillary effect and gas dissolution phenomena are considered in the numerical model. The effects of the feature size, imprint pressure, and ambient pressure were investigated in terms of time required to complete feature-filling steps.

3.2. Analysis model

As the analysis model, a liquid resin filling into pillar cavities was considered (see Figure 45). The resin-filling model is illustrated in Figure 46. In the figure, θ_p , R_p , h_p , h_R , and l_0 are the contact angle with regard to the pore surface, pore radius, pore height, residual layer thickness, and bulk domain radius, respectively.

In the analysis model, the rate of fluid filling into the pores on template v_{zp} can be estimated using the Hagen-Poiseuille law, which describes a slow viscous incompressible flow through a constant circular cross-section :

$$V_{zp}(t) = \frac{R_p^2}{8\mu h_f(t)} (P_{bulk} - P_s(t)) \quad (3.1)$$

Here, P_{bulk} and P_s are the bulk pressure and the pressure at the liquid surface inside the pore. These are defined as follows:

$$P_{bulk} = P_{amb} + P_{imp} \quad (3.2)$$

$$P_s(t) = P_{gas}(t) - \frac{2\gamma \cos \theta}{R_p} \quad (3.3)$$

Meanwhile, P_{gas} in equation (3.3) is the pressure of the entrapped gas in the pore, which is defined as

$$P_{gas}(t) = \frac{N_{gas}(t)RT}{V_{gas}(t)} = \frac{N_{gas}(t)RT}{\pi R_p^2 (h_p - h_f(t))} \quad (3.4)$$

where, N_{gas} , V_{gas} , R , and T are the number of gas molecules, the gas volume, the gas constant, and the gas temperature, respectively.

At the onset of feature-filling, the resin fills in the feature cavity, compressing the entrapped gas until P_{bulk} is greater than P_s . When the entrapped gas is fully compressed by the imprint and capillary forces, the gas molecules start to dissolve into the liquid resin. The pressure inside the gas decreases and the liquid level rises again. The gas dissolution and compression processes are repeated until the gas is dissolved completely in the numerical analyses.

The rate of change in number of moles of a gas is dependent on the gas concentration gradient at the liquid surface inside the feature. Assuming the gas concentration in the resin is linear in the z direction inside the pore, the rate of change in the number of moles can be given as follows:

$$\begin{aligned}
\frac{\partial N_{gas}}{\partial t} &= -\pi R_p^2 D \left. \frac{\partial n}{\partial z} \right|_{z=h_R+h_p} \\
&= -\pi R_p^2 D \left(\frac{n_s(t) - n_{bulk}}{h_f(t)} \right) \\
&= -\pi R_p^2 D \left(\frac{P_{gas}(t)C_h - n_{bulk}}{h_f(t)} \right)
\end{aligned} \tag{3.5}$$

The initial conditions for the analyses are shown below:

$$N_{gas}(0) = \frac{P_{amb} \pi R_p^2 h_f}{RT} \tag{3.6.a}$$

$$n_{bulk}(r, 0) = P_{amb} C_h \tag{3.6.b}$$

$$P_{gas}(0) = P_{amb} \tag{3.6.c}$$

3.3. Numerical result

The process parameters used in the feature-filling analyses are given in Table 3. The

parameter values in Table 3 were used for all feature-filling analyses in this chapter unless otherwise noticed. Figure 47 depicts the time evolution of feature-filling ratio, which is defined as h_f / h_p . From the result, it is notable that the initial feature-filling process occurs sooner by orders of magnitude than the remainder of the filling. This difference in the feature-filling time scale is due to the initial low pressure of the gas in the pores. In addition, Figure 47 shows the effect of the capillary force. Ignoring the capillary effect in the analysis, the compression rate of the entrapped gas is much lower than that including the capillary effect. That is, the entrapped gas is compressed by both the imprint pressure and the capillary pressure together during the SFIL process, enhancing the solubility of the gas into the resin.

As a parameter study, the effects of the pore radius, pore height, imprint pressure, and ambient gas reduction were investigated. Figures 48 and 49 present the evolution of feature-filling ratio and filling completion time with respect to the pore radius, respectively. The result shows that it takes longer to fill pores with larger diameters than it does to fill pores with smaller diameters, owing to the lower capillary forces associated with pores with larger diameters.

Figures 50 and 51 show the feature-filling analysis results with respect to the pore height. As both the imprint pressure and capillary pressure are identical in all cases, a taller pore requires a longer filling time.

Figures 52 and 53 present the results with respect to the imprint pressure. As the imprint pressure increases, the gas dissolution time decreases. However, the effects of the imprint pressure are not particularly significant for the analysis cases. That is, when the imprint pressure increased eight times from 0.125 atm to 1atm, the gas dissolution time decreased only by 44 percent, from 22.2 seconds to 12.5 seconds.

Last but not least, the effect of a reduction in the ambient gas was investigated. Figures 54 and 55 shows that the gas dissolution time decreased significantly as the ambient gas pressure decreased. The dissolution time of an entrapped gas is absolutely dependent on the total amount of gas molecules inside the feature cavity. Therefore, a reduction of the ambient gas pressure can be a positive means of reducing the feature-filling time. However, as UV-curable resins are generally very volatile, reduction of the ambient gas results in rapid resin evaporation.

3.4. Conclusion

The characteristics of feature-filling in the SFIL process were studied numerically in this chapter. When imprinting micro- or nano-scale features, the capillary force enhances both the liquid rise into the cavity and entrapped gas dissolution. Therefore, features with larger diameters take longer to fill than those with smaller diameters. In addition, when the depth of a feature cavity is deeper, it takes more time for the

entrapped gas to be dissolved, as there are more gas molecules entrapped in cavities with deeper features.

An increase in the imprint pressure and a decrease of the ambient pressure can help reduce the entrapped gas dissolution time. However, because most UV-curable resins are volatile, a reduction in the ambient gas pressure could result in resin evaporation, even before the mold starts to press the resin droplets.

Chapter 4 Demolding process

4.1. Research background

After the UV-curing process in SFIL, the mold template and imprinted polymer pattern are separated. However, during the demolding process, the final structures released from the mold template can be damaged by the adhesion and friction forces between the mold and pattern surfaces. In this case, some parts of the imprinted structure can become stuck to the template surface and be torn off.

There have been numerous efforts to reduce the structural failure caused by the demolding process in SFIL. Beck et al. [32] improved the anti-adhesion properties of Si- or SiO₂-based stamps by binding fluorinated silanes covalently the surface. Chan-Park and Neo [33] investigated the effects of important parameters, such as the roughness of mold, the taper angle of target structures, and the chemical interaction between the mold and polymer. Zhou and Chan-Park [34] studied the effects of UV irradiation on demolding forces for the fabrication of high-aspect-ratio micro-walls by UV NIL. Dai et al. [35] studied the adhesion properties of SU-8, a UV-curable negative resist resin. They measured the adhesion properties of cured SU-8 on metallic surface materials such as Au, Ti, Cu, Cr, and Ni. Garidel et al.[36] developed a technique to prevent the degradation of the anti-sticking layers in UV NIL. They used a self-assembled monolayer as an anti-sticking layer and modified their acrylate-based resist

by adjunction of a fluorine surfactant. They reported that almost no degradation of the anti-sticking layer was observed in terms of the surface energy and fluorine density after more than 50 prints. Kim et al.[37] also developed an anti-sticking resin obtained by mixing a fluorine-containing monomer to reduce the adhesion force during the demolding process in UV NIL.

Meanwhile, Tallal et al.[38] measured the approach–retract force curves for various polymers by means of AFM nano-indentation. Their experimental result presented that the force to pull-off the AFM tip from the polymers decreases significantly when using an anti-adhesion coating. A similar work was conducted by Cameron et al. [39]. They used AFM tips which were silanized with four different self-assembling monolayers. A variable-temperature chemical force microscope was used to measure the pull-off forces of AFM tips from a thin polymer film at a series of temperatures. The result showed that a self-assembled monolayer decreases the adhesion force, whereas the adhesion force increases substantially at the glass-transition temperature of the polymer. Kawata et al. [40] measured the demolding forces of Si molds with various side wall profiles. Their results showed that when the template has tapered and smooth side walls, the demolding force decreases significantly.

Many research groups have attempted numerical approaches with finite element methods to analyze the demolding process in NIL [41, 42]. Worgull et al. [43] predicted the stress distribution during large-area embossing by finite element

simulation. The result presented that, in order to avoid an inhomogeneous pressure distribution in the polymer flow and achieve uniform shrinkage over the entire pattern area, it is critical to restrict the pattern area with shrinkage barriers. Guo et al. [15] also noted that the main factors which lead to structural damage during demolding are the mismatch between the thermal expansion coefficients, the adhesion force, and the friction force on the interface. They also correlated the adhesion force and the surface energy of the two contact surfaces quantitatively by an empirical formula based on elasto-plastic contact. Chan-Park et al. [44] investigated the stress distribution in UV-cured high-aspect-ratio patterns during a demolding process. They formed a cohesive zone model on the interface between the mold and the polymer. They also included the cross-linking shrinkage of the polymer in the simulation. Although their attempt to use the cohesive zone model was reasonable, the mesh size they used was too large such that there could have been significant numerical errors [45].

However, there have not yet been proper simulation tools or techniques developed for an accurate analysis of the demolding process. Therefore, it is meaningful to develop a simulation technique which can give reasonable results and help us understand the demolding process. In this chapter, the demolding process was analyzed by the finite element methods using a cohesive zone model to determine which process parameters are more important in the demolding process. The commercial finite element code ABAQUS/Standard was used as the analysis tool.

The effects of the pattern shape and shrinkage rate on the demolding process were closely investigated.

4.2. Experiment

The demolding forces were measured by commercial SFIL equipment, specifically the Imprio-100 SFIL system (Micro Imprints Inc., U.S.), while imprinting typical line and space patterns. The load cells embedded in the UV imprint system were used to measure the imprint forces.

Silicon master molds with various line and space patterns were prepared for the experiments. The geometries and scanning electron microscope (SEM) images of the master mold cross sections are given in Figure 56. The pattern pitch varies from 1 μm to 4 μm , while the pattern height varies from 250nm to 1 μm .

Figure 57 illustrates the demolding test procedure. First, a soft polymer mold is replicated from a Si master mold. Before replicating the soft mold, an anti-adhesion layer is coated onto the Si master mold surface. 'Relmat', provided by Micro Imprints Inc. in the U.S., was used as the anti-adhesion coating material in this research. Then, a UV-curable liquid resin is introduced onto the master mold surface. 'Monomat', which was also provided by Micro Imprints Inc., was used as the UV-curable resin in this

study. Next, a flat quartz template was used to press the liquid resin. This was followed by an UV exposure. Upon the completion of the UV-curing process, the replicated soft mold is released from the Si master mold. Figures 58 (a) and (b) show images of the quartz template before and after replication of the master mold pattern, respectively.

Next, the demolding forces are measured while imprinting line and space patterns using the soft mold replicated from the master mold. Before the imprinting process, an anti-adhesion coating is applied to the soft mold surface with 'Relmat'. Then the UV curable resin 'Monomat' is applied onto a silicon wafer before it is pressed by the soft mold. After the UV-curing process, the demolding force is measured by three load cells pre-equipped in the SFIL system while the imprinted pattern is released from the soft mold.

Figure 59 shows SEM images of cross-sections of the imprinted patterns with various pattern heights and pitches. The results of the demolding force measurement are given in Figures 60 and 61. Figure 60 shows that as the pattern height becomes taller, the required demolding force also increases. Meanwhile, the demolding force decreases as the pattern pitch increases, as shown in Figure 61. From these results, it can be concluded that the total area of the side wall has a significant effect on the demolding force in NIL, as the friction and adhesion forces increases in proportional to the side wall area.

4.3. Analysis model

The demolding processes in SFIL were investigated by finite element analysis as well. The commercial finite element analysis code ABAQUS/standard was used for the analysis. A cohesive zone model(CZM) [45] was applied to the interface between the mold template and the imprinted pattern to present adhesion effects. A bilinear relationship between the tractions and the displacement jumps was applied to the CZM used in this study (see Figure 62). K , τ^0 , G_C , and Δ denote the interface stiffness, interfacial strength, critical fracture energy per unit area (or work of adhesion), and opening displacement, respectively.

The relationship between normal and tangential interface stiffness was assumed to be

$$K_t = \frac{K_n}{2(1+\nu)} \quad (4.1)$$

where, 't' and 'n' in subscript represent tangential and normal, respectively.

Meanwhile, the relationship between the normal and tangential interfacial strengths was assumed as follows:

$$\tau_t^0 = \frac{\tau_n^0}{\sqrt{3}} \quad (4.2)$$

A power-law-based damage evolution criterion was used for crack propagation, as follows:

$$\left(\frac{G_I}{G_{IC}}\right)^2 + \left(\frac{G_{II}}{G_{IIC}}\right)^2 = 1 \quad (4.2)$$

G_I , G_{IC} , G_{II} , and G_{IIC} are the normal, critical normal, tangential, and critical tangential fracture energies per unit area, respectively.

The normal interfacial strength was experimentally measured and determined to be 0.159MPa. However, the interfacial fracture energies are almost impossible to measure, because the crack opening occurs in a much shorter time than the measuring time interval of the mold position sensor. Therefore, based on the normal interfacial strength which could be achieved, various cohesive zone models with different interface stiffness and fracture energies were tried as candidate CZMs (see Figure 63).

Meanwhile, the simulation models used material properties of 10% volumetric shrinkage, a 100MPa elastic modulus, and a Poisson's ratio of 0.4, respectively [46]. Figure 64 is a typical example of a finite element model for demolding analysis of a line and space patterning. Figure 65 is an example of the demolding simulation result. The element size at the interface between the mold and imprinted pattern was determined to be 15nm.

To confirm which CZM in Figure 63 is suitable for analysis, simulation results with

all CZMs in Figure 63 were compared to the experimental result shown in Figure 60. As presented in Figure 66, the result with the CZM that is specified in Figure 67 (case 'G' in Figure 63) shows the best agreement with the experimental result.

4.4. Numerical result

Demolding simulations of line and space patterning by SFIL were conducted. Figure 68 and 69 are stress contours obtained by the demolding simulations for various pattern heights and pattern pitches, respectively. The experimental and numerical results with respect to the pattern height are compared in Figure 70. The line width, line interval, and residual layer thickness were 500nm, 1000nm, and 50nm respectively. As the pattern height increased from 250nm to 1000nm, the demolding force per unit area increased by about 50% from 0.197MPa to 0.315MPa almost linearly. In addition, a sharp stress concentration appears at the roots of the line structures. This stress concentration is mainly caused by cross-link shrinkage, but the stress level increases as the pattern height becomes taller. Figure 71 shows the maximum stresses at the root while releasing the mold with respect to the pattern height. The maximum stress at the root increased by only about 7% as the pattern height increased from 250nm to 1000nm.

Figure 72 shows a comparison of demolding forces from the experimental and

numerical results with respect to the pattern pitch. The pattern pitches were 1 μm , 2 μm , and 4 μm , respectively. Meanwhile, the pattern width and pattern height were 500nm and 1 μm , respectively. As the pattern pitch increased, the demolding force per unit area decreased, because the total friction force or adhesion force at the side walls was reduced. However, as shown in Figure 73, the decrease of pattern pitch increased the maximum stress at the line root, as wider patterns are affected much more than the narrow patterns by the cross-link shrinkage.

The effects of cross-link shrinkage on the demolding process were investigated. Figure 74 shows stress contours and deformed shapes of a line structure after volumetric shrinkage rates of 10% and 20%, respectively. The line structure had the following dimension: a 500nm width, a 500 nm height, and a 1000nm interval. As presented in Figure 75, the demolding force decreases when the cross-link shrinkage rate increases. That is, the cross-link shrinkage helps release the mold in SFIL. However, the stress at the root of the line structure increases as the shrinkage rate increases. Figure 76 depicts the relationship between the shrinkage rate and shrinkage stress.

One of the issues associated with the NIL demolding process is shrinkage mismatch. For example, during the thermal NIL process, the mold, the substrate, and the resist material have different thermal expansion coefficients. Therefore, shrinkage mismatch

is inevitable in the cooling process before the demolding process. Moreover, the shrinkage mismatch negatively affects the imprint quality [15]. However, in a UV NIL process such as SFIL, the substrate and mold do not experience any shrinkage, as there are no significant temperature changes in the UV-curing process. Meanwhile, only the polymer cured by UV rays shrinks due to the cross-linking process. Therefore, the effects of shrinkage mismatch are expected to be insignificant in SFIL. To verify this phenomenon, numerical simulations of pattern shrinkage with various residual layer thicknesses were conducted. Figure 77 shows an example of the simulation model and its boundary conditions. Figure 78 presents the numerical results of the pattern shrinkage, with the stress distribution contours presenting that the edges of the imprinted patterns are affected by cross-link shrinkage. In addition, as the residual layer thickness increases, the affected zone also becomes larger. However, the affected zone is limited to a few line structures. Thus, shrinkage mismatch is not a serious problem in UV NIL.

Setting aside shrinkage mismatch issue, other types of eccentricities between the mold and the imprinted structure can occur during the demolding process. For example, the mold can be tilted or shifted in unwanted directions by mechanical tolerance or control errors. The effects of this type of mold eccentricity were investigated by numerical simulations. In these simulations, the mold moved to the left by 20nm after the line pattern shrunk by 10 percent. Figure 79 shows stress contours and deformed

shapes of the imprinted mold after the shifting of the mold. As shown in Figure 80, the maximum stress in the imprinted structure increases as the mold shifts further. Moreover, when using a hard mold, the effects of mold shift on the imprinted structure are much more significant than they are when using a soft mold. In this study, the hard mold was assumed to be quartz, while the soft mold was assumed to be the replicated mold with the UV-curable resin.

Finally, the demolding processes of partially filled structures were studied. A line pattern with a 500nm width, a 500nm height, and a 1000nm pitch was considered. Figure 81 shows the stress distributions in partially filled line patterns during the demolding process. Demolding forces associated with the filling ratios are given in Figure 82. The result shows that the demolding force increases linearly as the filling ratio increases. However, it is notable that when the filling ratio reaches 100% the demolding force increases suddenly, as the top of the pattern is attached at that point to the mold.

4.5 Conclusion

Demolding processes of line and space patterning with SFIL were successfully demonstrated by a finite element analysis using a cohesive zone model. The effects of pattern geometries such as pattern heights and pitches on the demolding force were

investigated by a numerical analysis technique. The results showed that the demolding force increases as the pattern height becomes taller or as the pattern pitch becomes wider.

The cross-link shrinkage of the UV-curable resin was also considered. It was shown that the cross-link shrinkage helps reduce the demolding force. However, the stress level increased as the shrinkage rate increased. Additionally, in contrast to the thermal NIL process, thermal expansion was not noted in either the mold or the substrate for UV NIL. Therefore, the effects of shrinkage mismatch in the UV NIL were insignificant.

Other parameter studies such as a mold shift during the demolding process and the effects of partial feature-filling on the demolding process were carried out as well. The imprinted pattern was significantly affected by the mold shift. The stress level in the imprinted pattern increased as the shift distance from the mold increased. Meanwhile, the demolding forces for partially filled patterns were lower than those of fully filled patterns owing to the reduction of the interfacial area in the partially filled patterns.

Summary

A step and Flash Imprint Lithography (SFIL) process using UV-curable resins was studied. A numerical code was developed to analyze the resin droplet behaviors and gas void entrapment characteristics during the SFIL. The process of resin filling into the feature cavities was also analyzed numerically. The demolding process was demonstrated by a finite element method using a cohesive zone model.

Four different resin-dispensing recipes were compared in terms of both the spreading time and residual layer thickness. For most recipes, the resin-spreading time increased drastically as the residual layer thickness became thinner. Meanwhile, the zigzag recipe was not limited by the residual layer thickness. However, gas void entrapment was inevitable for the zigzag recipe. To avoid defects induced by an entrapped gas void, droplets with small volumes and shorter dispensing intervals should be applied to reduce the gas void dissolution time.

In SFIL, the capillary force enhances both the rise of the liquid resin into the feature cavity and dissolution of the entrapped gas inside the feature cavity. Therefore, features with larger characteristic dimensions take more time to fill themselves with the liquid resin. In addition, an increase in the imprint pressure and a decrease of the ambient pressure can help reduce the entrapped gas dissolution time. However, because most UV-curable resins are volatile, a reduction of the ambient gas pressure could result in resin evaporation.

The demolding process during the fabrication of line and space structures was investigated. The result showed that the demolding force increased as the pattern height became taller or as the pattern pitch becomes wider. Meanwhile, the cross-link shrinkage of the UV-cured pattern helped reduce the demolding forces in the SFIL process, in which neither the mold nor the substrate experience any shrinkage.

Using the numerical analysis techniques developed in this study, the main processes of SFIL were successfully analyzed. These techniques can be applied to other UV NIL processes as well. They can be used to optimize UV NIL processes, leading to a reduction of the design and production costs.

References

1. Gates, B.D., et al., *New approaches to nanofabrication: molding, printing, and other techniques*. Chemical reviews, 2005. **105**(4): p. 1171-1196.
2. Campbell, S.A., *The science and engineering of microelectronic fabrication*. Vol. 476. 1996: Oxford University Press New York.
3. Chou, S.Y., P.R. Krauss, and P.J. Renstrom, *Nanoimprint lithography*. Journal of Vacuum Science & Technology B: Microelectronics and Nanometer Structures, 1996. **14**(6): p. 4129-4133.
4. Stewart, M.D. and C.G. Willson, *Imprint materials for nanoscale devices*. MRS bulletin, 2005. **30**(12): p. 947-951.
5. Chou, S., et al., *Sub-10 nm imprint lithography and applications*. Journal of Vacuum Science & Technology B: Microelectronics and Nanometer Structures, 1997. **15**(6): p. 2897-2904.
6. Michaelson, T., et al. *Step and flash imprint lithography: a new approach to high-resolution patterning*. in *Microlithography'99*. 1999. International Society for Optics and Photonics.
7. Bailey, T., et al., *Step and flash imprint lithography: An efficient nanoscale printing technology*. Journal of Photopolymer Science and Technology, 2002. **15**(3): p. 481-486.
8. Tan, H., A. Gilbertson, and S. Chou, *Roller nanoimprint lithography*. Journal of Vacuum Science & Technology B: Microelectronics and Nanometer Structures, 1998. **16**: p. 3926.
9. Ahn, S.H. and L.J. Guo, *High-Speed Roll-to-Roll Nanoimprint Lithography on Flexible Plastic Substrates*. Advanced materials, 2008. **20**(11): p. 2044-2049.
10. Ahn, S. and L. Guo, *Large-Area Roll-to-Roll and Roll-to-Plate Nanoimprint Lithography: A Step toward High-Throughput Application of Continuous Nanoimprinting*. ACS nano, 2009. **3**(8): p. 2304-2310.

11. Zankovych, S., et al., *Nanoimprint lithography: challenges and prospects*. Nanotechnology, 2001. **12**: p. 91.
12. Resnick, D.J., S. Sreenivasan, and C.G. Willson, *Step & flash imprint lithography*. Materials Today, 2005. **8**(2): p. 34-42.
13. Malloy, M. and L.C. Litt, *Technology review and assessment of nanoimprint lithography for semiconductor and patterned media manufacturing*. Journal of Micro/Nanolithography, MEMS, and MOEMS, 2011. **10**(3): p. 032001-032001-13.
14. Peng, Z., et al., *The properties of demoulding of Ni and Ni-PTFE moulding inserts*. Sensors and Actuators A: Physical, 2005. **118**(2): p. 338-341.
15. Guo, Y., et al., *Study of the demolding process—implications for thermal stress, adhesion and friction control*. Journal of Micromechanics and Microengineering, 2006. **17**(1): p. 9.
16. Colburn, M., et al., *Ramifications of lubrication theory on imprint lithography*. Microelectronic Engineering, 2004. **75**(3): p. 321-329.
17. Batchelor, G., *An Introduction to Fluid Mechanics* (Cambridge. Press, Cambridge UK, 1967.
18. Reddy, S. and R.T. Bonnecaze, *Simulation of fluid flow in the step and flash imprint lithography process*. Microelectronic Engineering, 2005. **82**(1): p. 60-70.
19. Hirt, C.W. and B.D. Nichols, *Volume of fluid (VOF) method for the dynamics of free boundaries* 1*. Journal of computational physics, 1981. **39**(1): p. 201-225.
20. Schmitt, H., et al., *UV nanoimprint materials: Surface energies, residual layers, and imprint quality*. Journal of Vacuum Science & Technology B, 2007. **25**(3): p. 785-790.
21. Kim, K., et al., *Minimization of residual layer thickness by using the optimized dispensing method in S-FIL process*. Microelectronic Engineering, 2006. **83**(4): p. 847-850.

22. Liang, X., et al., *Air bubble formation and dissolution in dispensing nanoimprint lithography*. Nanotechnology, 2007. **18**: p. 025303.
23. Usuki, K., et al. *Approaches to rapid resist spreading on dispensing based UV-NIL*. in *SPIE Advanced Lithography*. 2011. International Society for Optics and Photonics.
24. Baliga, B. and S. Patankar, *A control volume finite-element method for two-dimensional fluid flow and heat transfer*. Numerical Heat Transfer, Part A: Applications, 1983. **6**(3): p. 245-261.
25. Tucker III, C. and F. Folgar, *A model of compression mold filling*. Polymer Engineering & Science, 1983. **23**(2): p. 69-73.
26. De Gennes, P.-G., F. Brochard-Wyart, and D. Quéré, *Capillarity and wetting phenomena: drops, bubbles, pearls, waves*. 2004: Springer.
27. Lee, W.I., S.-H. Kang, and S.-W. Choi, *Dispensing method of resin for imprinting*. Korean patent, 2011. **Registration No. 101060360**
28. Cappelazzo, M., et al., *Stokes-Einstein relation for pure simple fluids*. The Journal of chemical physics, 2007. **126**(22): p. 224516.
29. Chauhan, S., et al., *Feature-filling modeling for step and flash imprint lithography*. Journal of Vacuum Science & Technology B: Microelectronics and Nanometer Structures, 2009. **27**(4): p. 1926-1932.
30. Yoneda, I., et al. *A study of filling process for UV nanoimprint lithography using a fluid simulation*. 2009.
31. Hirai, Y., *UV-nanoimprint lithography (NIL) process simulation*. Journal of Photopolymer Science and Technology, 2010. **23**(1): p. 25-32.
32. Beck, M., et al., *Improving stamps for 10 nm level wafer scale nanoimprint lithography*. Microelectronic Engineering, 2002. **61**: p. 441-448.
33. Chan-Park, M. and W. Neo, *Ultraviolet embossing for patterning high aspect ratio polymeric microstructures*. Microsystem technologies, 2003. **9**(6): p. 501-506.
34. Zhou, W. and M.B. Chan-Park, *Large area UV casting using diverse*

- polyacrylates of microchannels separated by high aspect ratio microwalls.* Lab on a Chip, 2005. **5**(5): p. 512-518.
35. Dai, W., K. Lian, and W. Wang, *A quantitative study on the adhesion property of cured SU-8 on various metallic surfaces.* Microsystem technologies, 2005. **11**(7): p. 526-534.
 36. Garidel, S., et al., *Improved release strategy for UV nanoimprint lithography.* Journal of Vacuum Science & Technology B: Microelectronics and Nanometer Structures, 2007. **25**(6): p. 2430-2434.
 37. Kim, J.Y., et al., *UV-curable nanoimprint resin with enhanced anti-sticking property.* Applied surface science, 2008. **254**(15): p. 4793-4796.
 38. Tallal, J., et al., *AFM characterization of anti-sticking layers used in nanoimprint.* Microelectronic engineering, 2006. **83**(4): p. 851-854.
 39. Cameron, N.S., et al., *Chemical force microscopy for hot-embossing lithography release layer characterization.* Soft Matter, 2006. **2**(7): p. 553-557.
 40. Kawata, H., et al., *Silicon template fabrication for imprint process with good demolding characteristics.* Microelectronic Engineering, 2009. **86**(4): p. 700-704.
 41. Worgull, M., M. Hecke, and W. Schomburg, *Large-scale hot embossing.* Microsystem technologies, 2005. **12**(1-2): p. 110-115.
 42. Worgull, M. and M. Hecke, *New aspects of simulation in hot embossing.* Microsystem Technologies, 2004. **10**(5): p. 432-437.
 43. Worgull, M., et al., *Modeling and optimization of the hot embossing process for micro-and nanocomponent fabrication.* Journal of Micro/Nanolithography, MEMS, and MOEMS, 2006. **5**(1): p. 011005-011005-13.
 44. Chan-Park, M.B., et al., *Simulation and investigation of factors affecting high aspect ratio UV embossing.* Langmuir, 2005. **21**(5): p. 2000-2007.
 45. Turon, A., et al., *An engineering solution for mesh size effects in the simulation of delamination using cohesive zone models.* Engineering

Fracture Mechanics, 2007. **74**(10): p. 1665-1682.

46. Johnson, S., et al., *Effects of etch barrier densification on step and flash imprint lithography*. Journal of Vacuum Science & Technology B: Microelectronics and Nanometer Structures, 2005. **23**(6): p. 2553-2556.

Figures

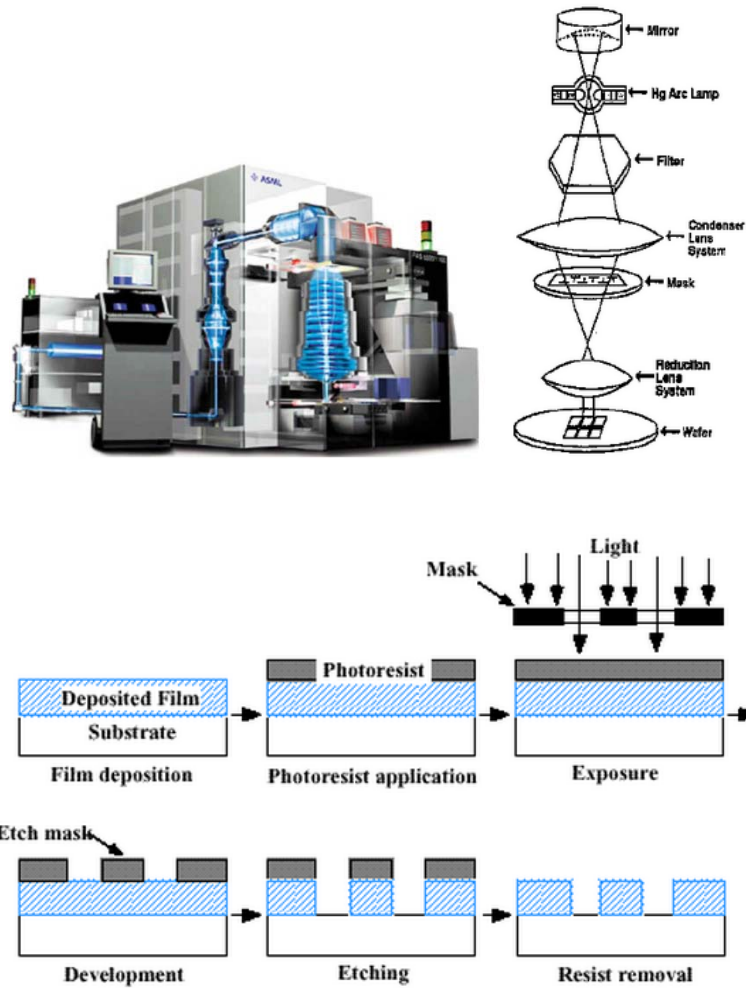


Figure 1 A typical photo lithography process
(<http://www.lrsm.upenn.edu/~frenchrh/lithography.htm>)

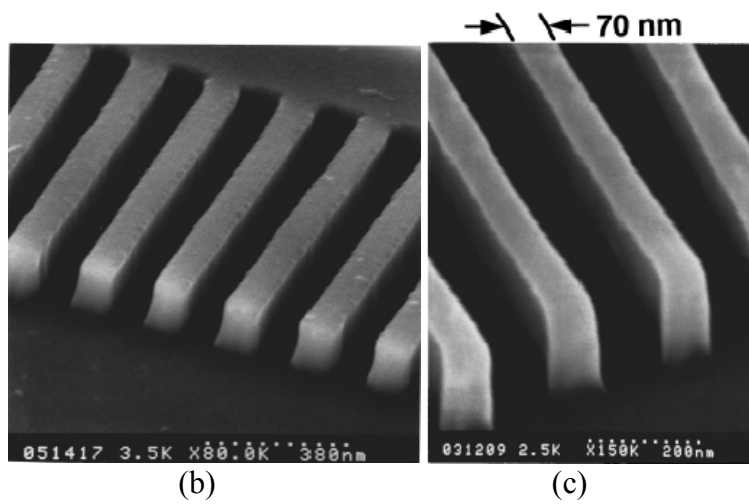
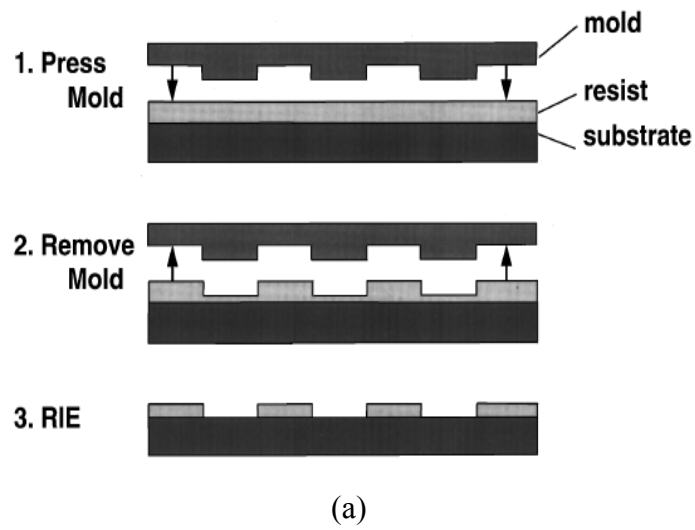


Figure 2 Nanoimprint lithography [3]: (a) a typical procedure of nanoimprint lithography (b) Si mold for a 70nm line pattern (c) 70nm PMMA line pattern imprinted with the Si mold

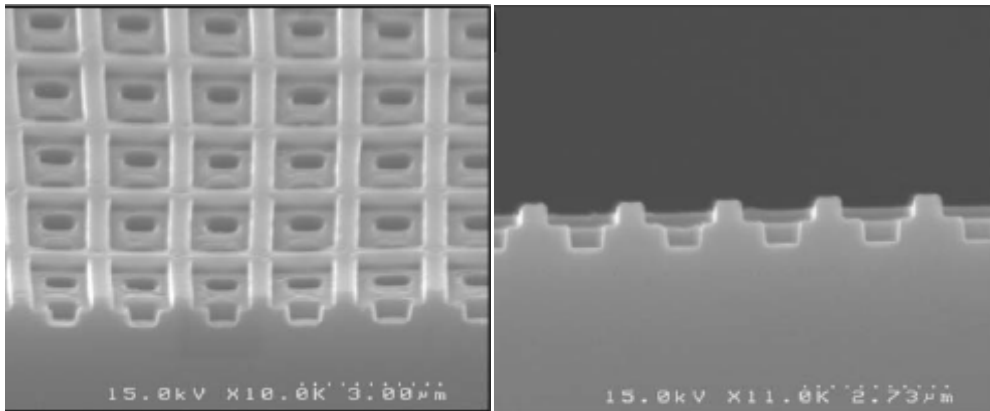


Figure 3 A three-dimensional pattern fabricated by the NIL process[4]

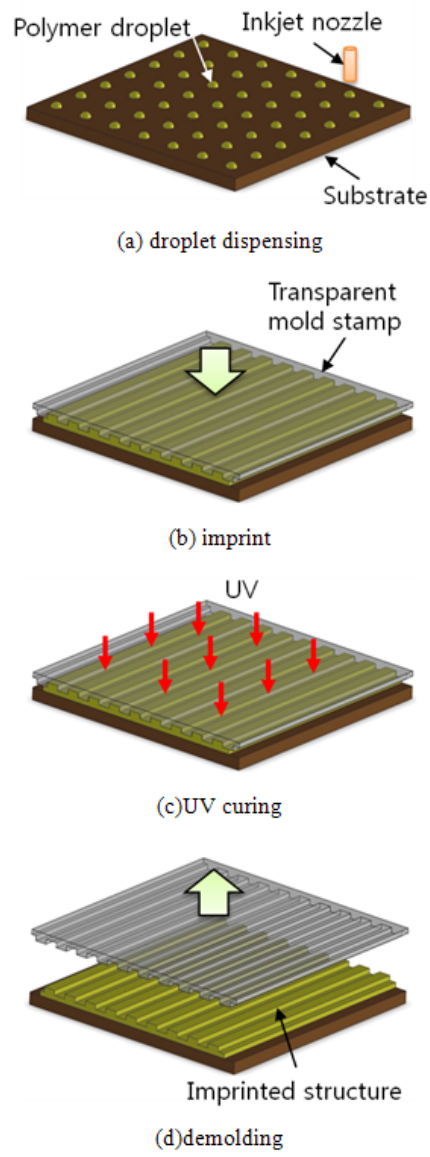


Figure 4 A typical procedure of step and flash imprint lithography (SFIL)

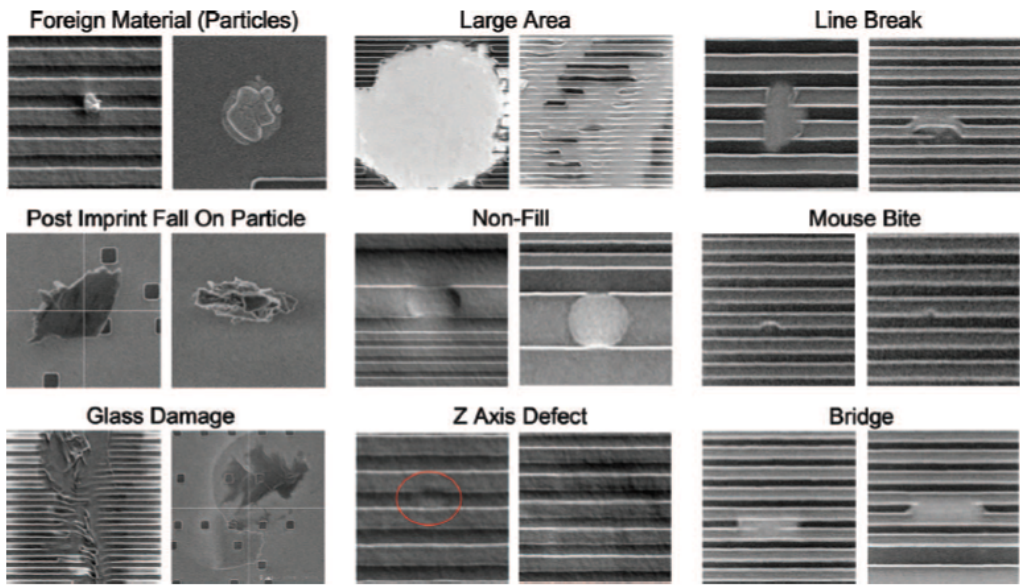


Figure 5 Examples of commonly observed defects in UV NIL [13]

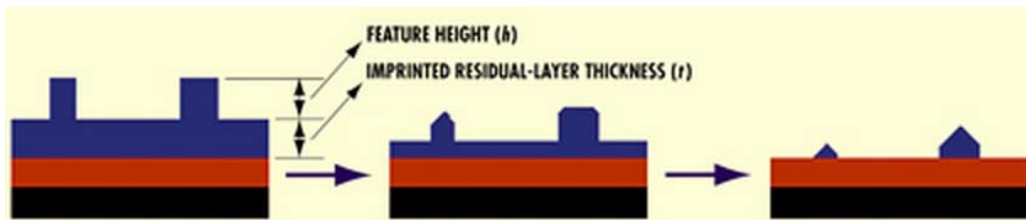


Figure 6 Removal of a residual layer and loss of feature dimension accuracy (<http://micromagazine.fabtech.org/archive/05/01/sreen.html>)

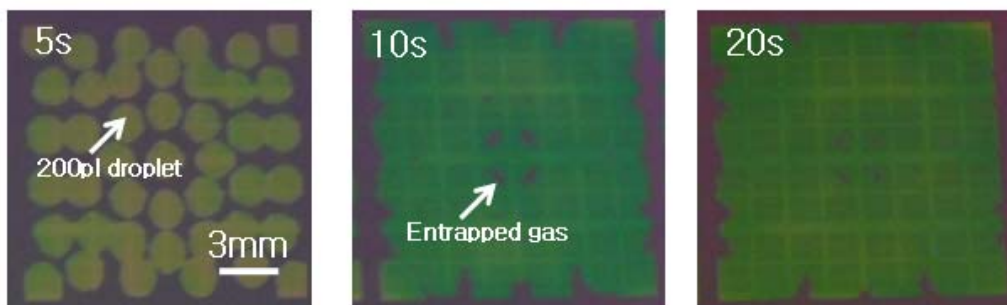


Figure 7 An example of resin droplet spreading and gas void entrapment in SFIL

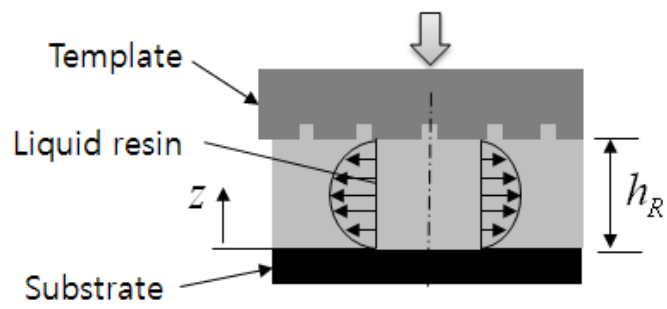


Figure 8 A schematic of liquid resin squeezed between the mold and substrate

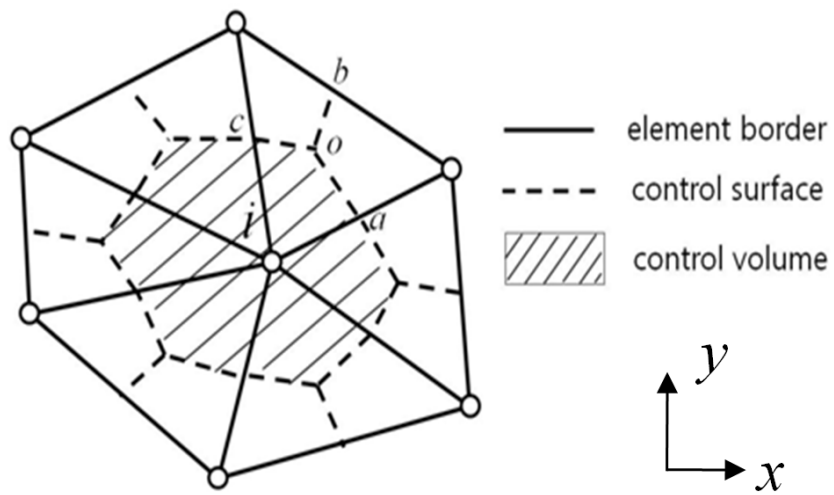


Figure 9 Configuration and notations of control volume used in CVFEM

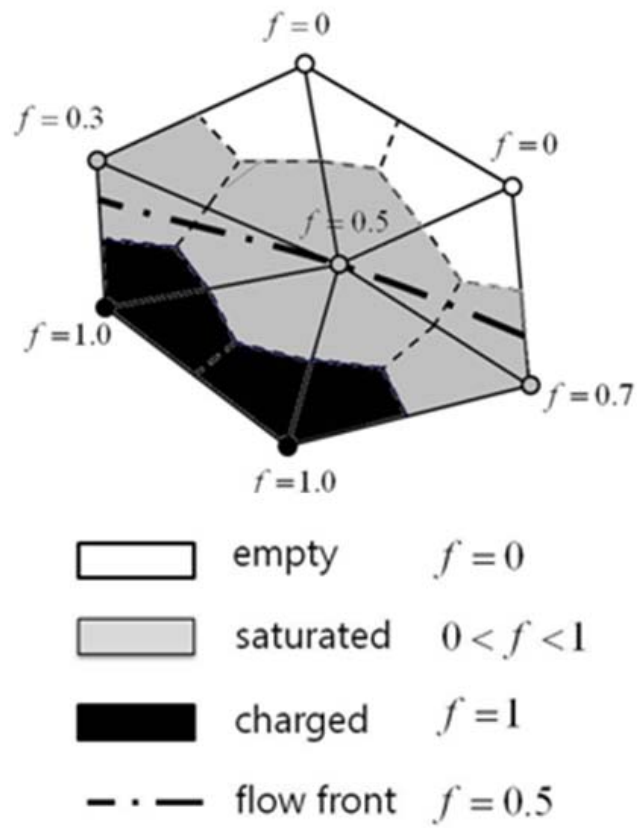


Figure 10 Concept of the volume of fluid (VOF) method

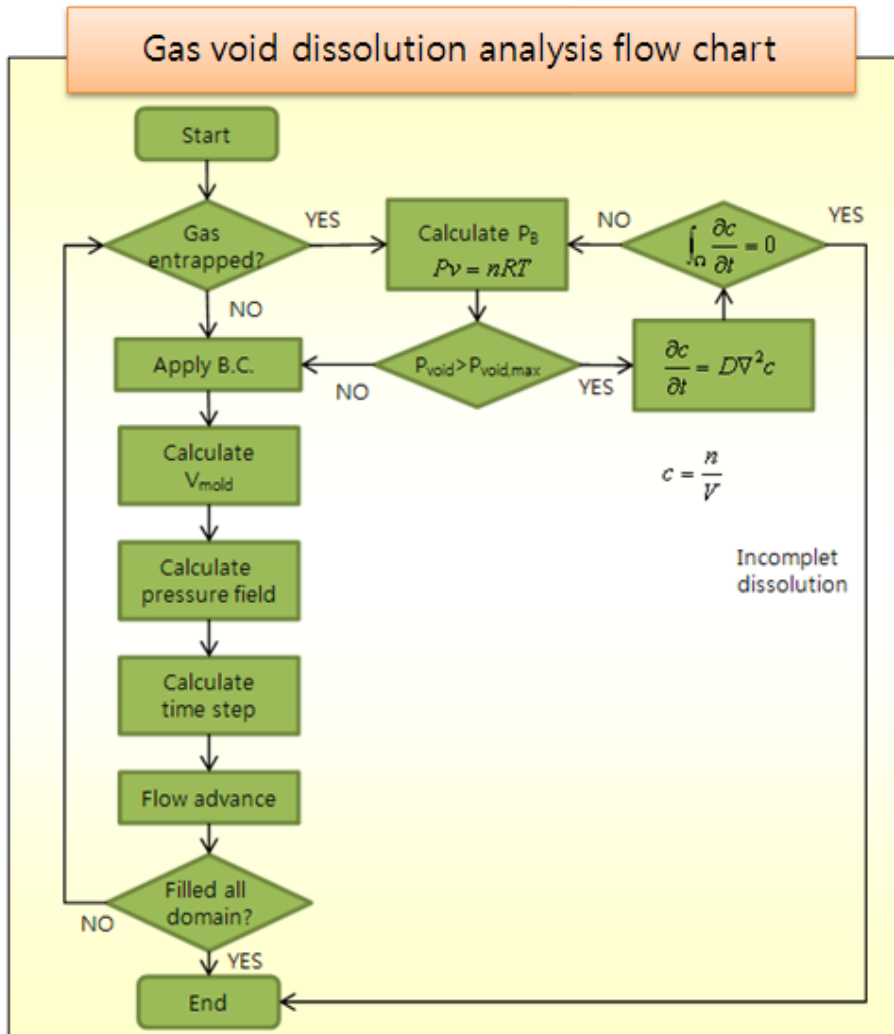


Figure 11 A flow chart for the gas void dissolution analysis



Figure 12 Imprio 100 S-FIL system (Molecular Imprints Inc., U.S.)

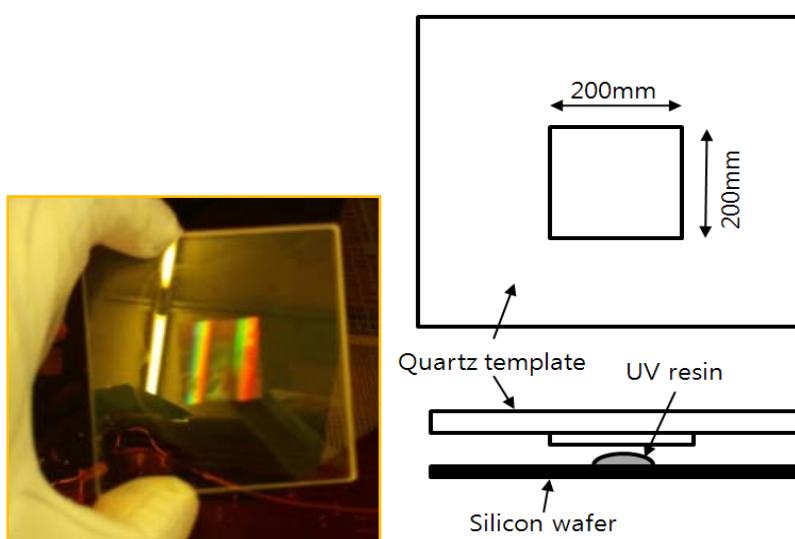


Figure 13 A quartz template used for Imprio 100 S-FIL system

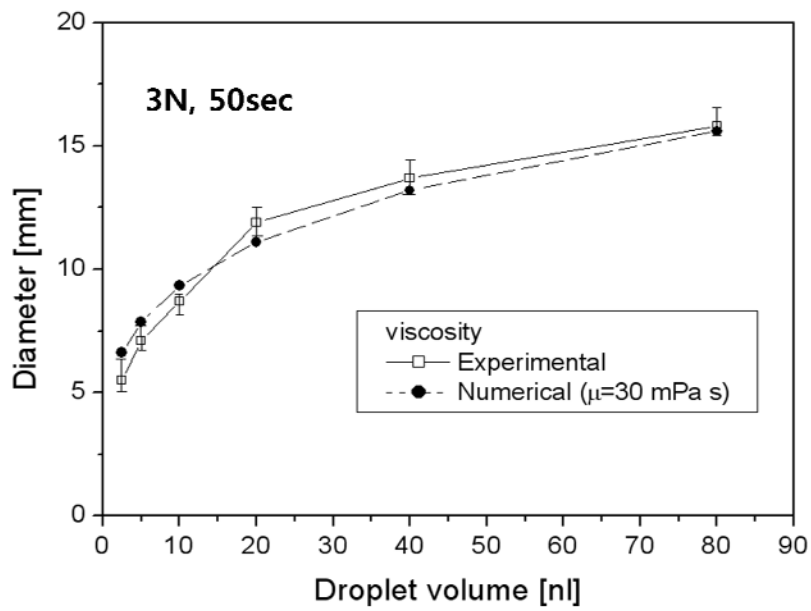
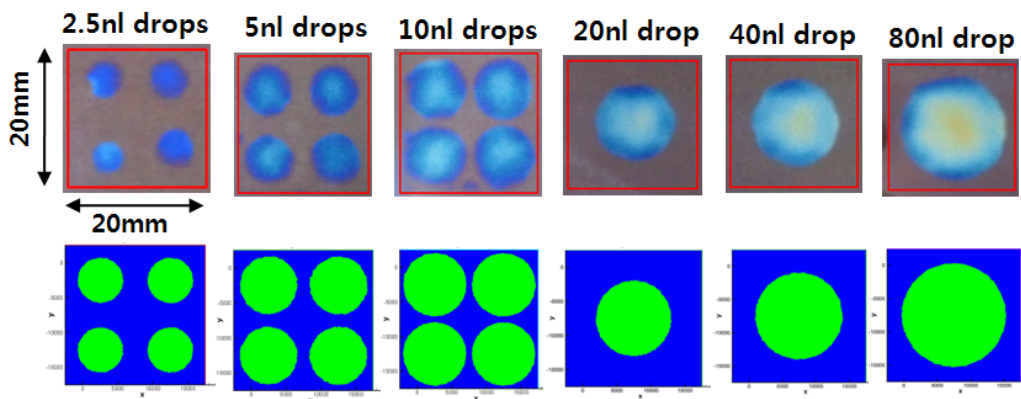


Figure 14 Comparison of droplet diameters for various volumes after being pressed by an imprint force of 3N for 50 seconds

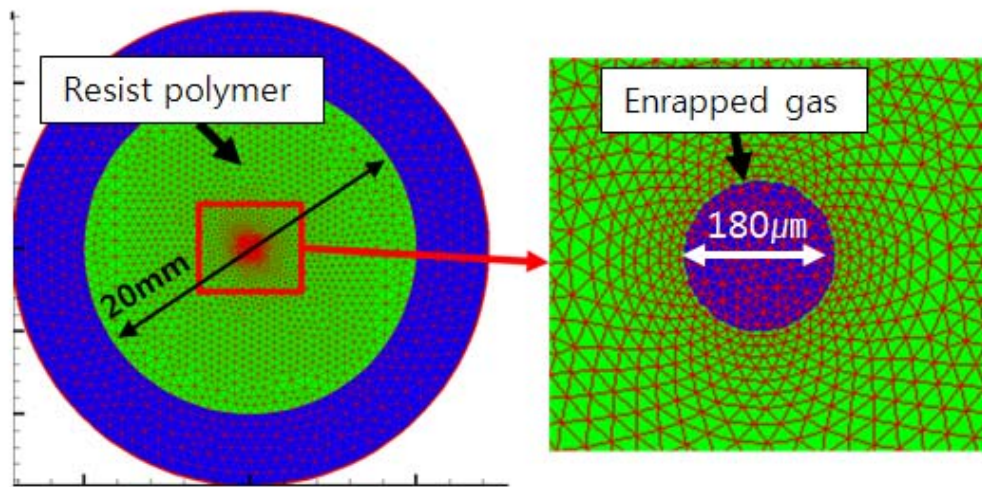
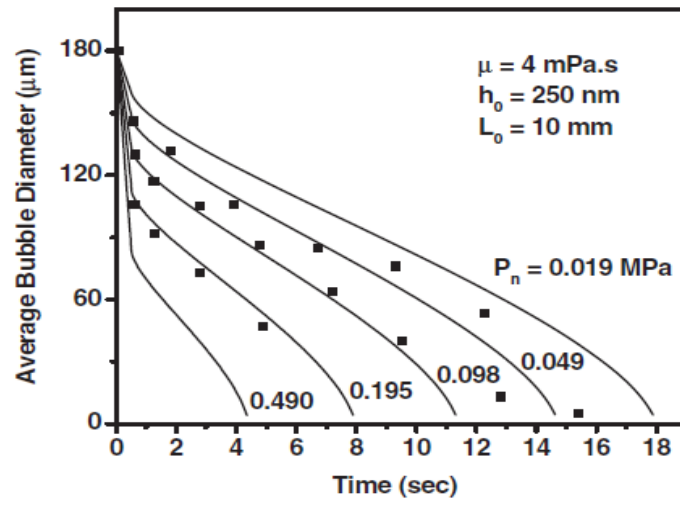
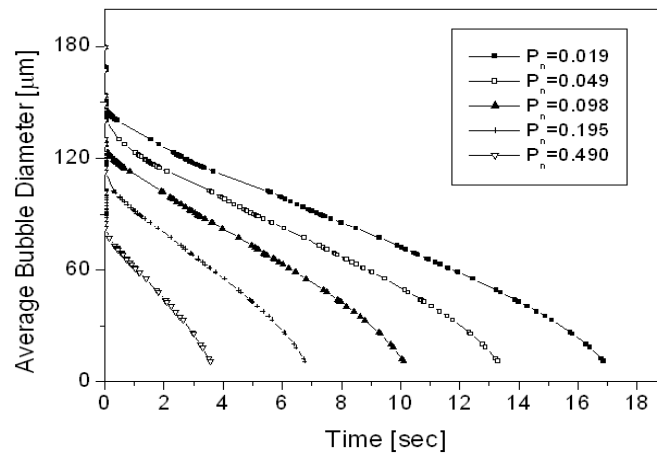


Figure 15 An analysis model of a gas void entrapped in the middle of a liquid resin film squeezed between two plates

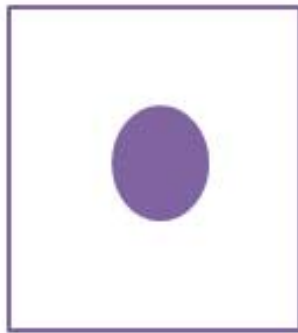


(a)

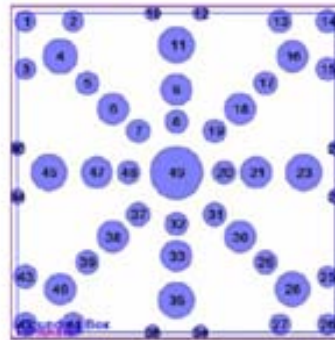


(b)

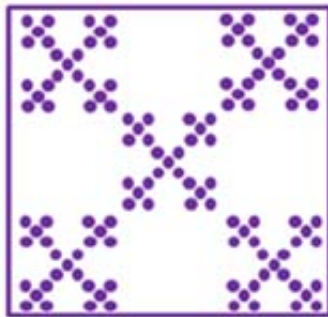
Figure 16 Time evolution of the void diameter for various imprint pressures: comparison of (a) results from [22] and (b) results with the numerical code developed in this study



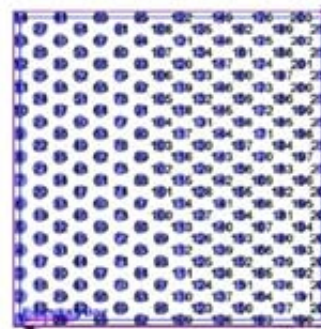
(a)



(b)



(c)



(d)

Figure 17 Droplet dispensing recipes: (a) single-drop, (b) spidergram, (c) repeated five drop, and (d) zigzag recipes.

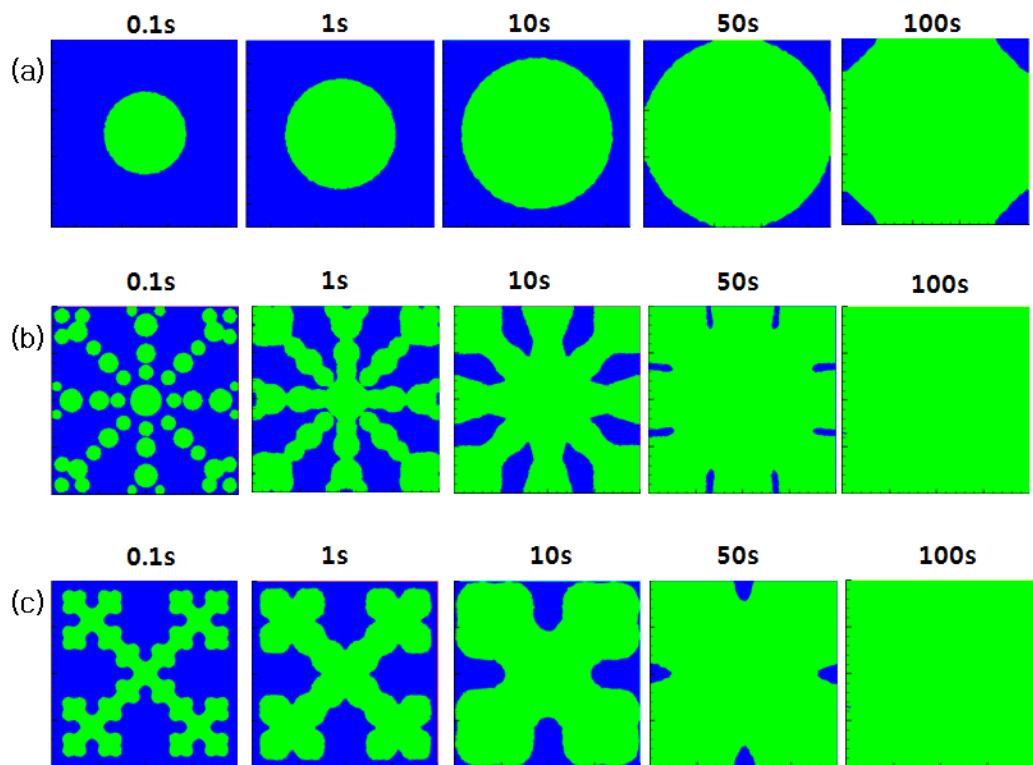
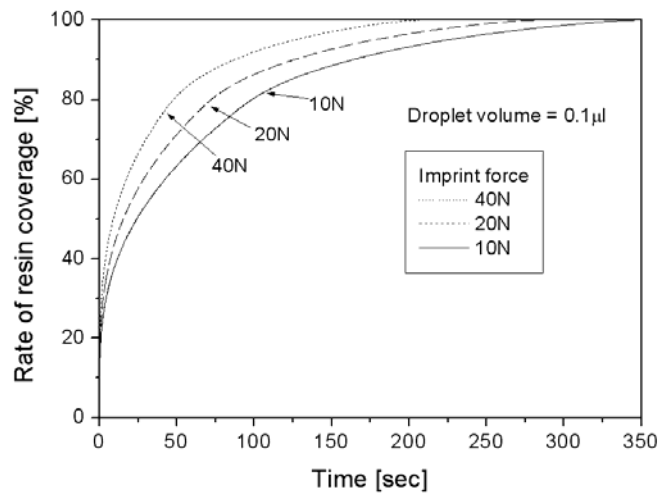
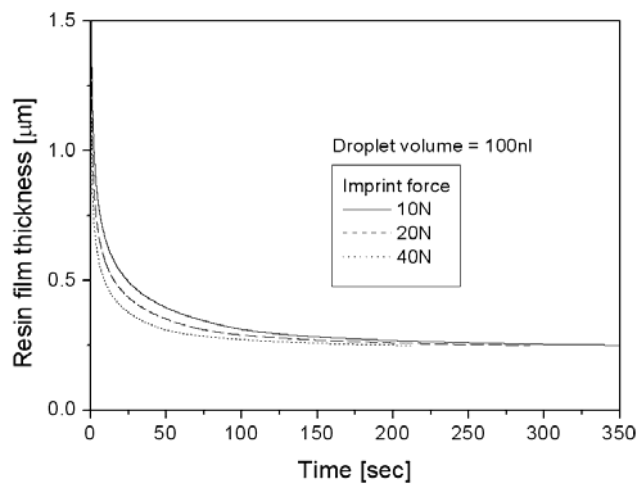


Figure 18 Examples of the resin-spreading simulation for three recipes: (a) single-drop, (b) spidergram, and (c) repeated five drop recipes

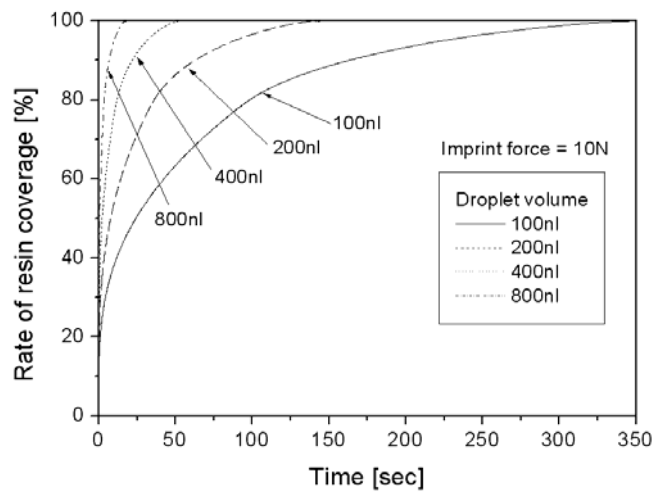


(a)



(b)

Figure 19 Time evolution of (a) the resin coverage rate and (b) resin film thickness with respect to the imprint force for the single-drop recipe



(b)

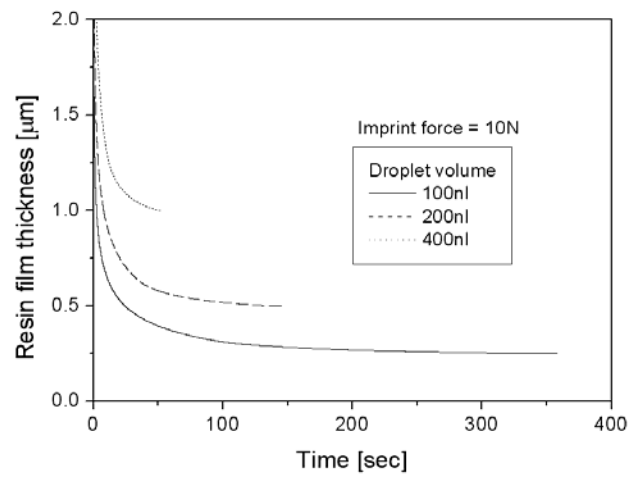


Figure 20 Time evolution of (a) the resin coverage rate and (b) resin film thickness with respect to the droplet volume for the single-drop recipe

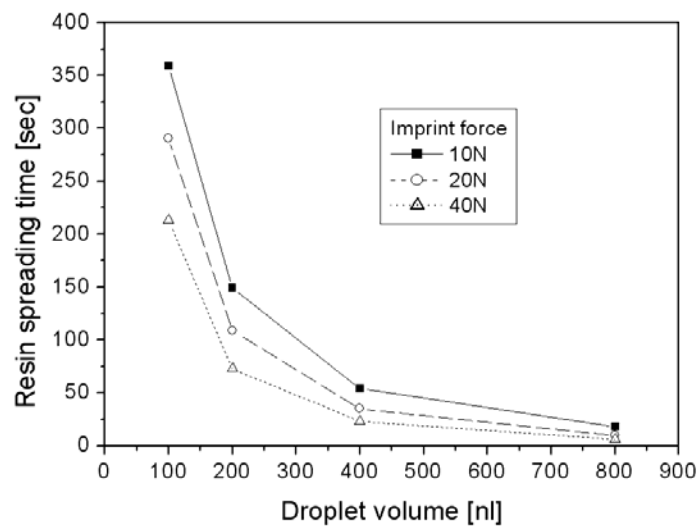
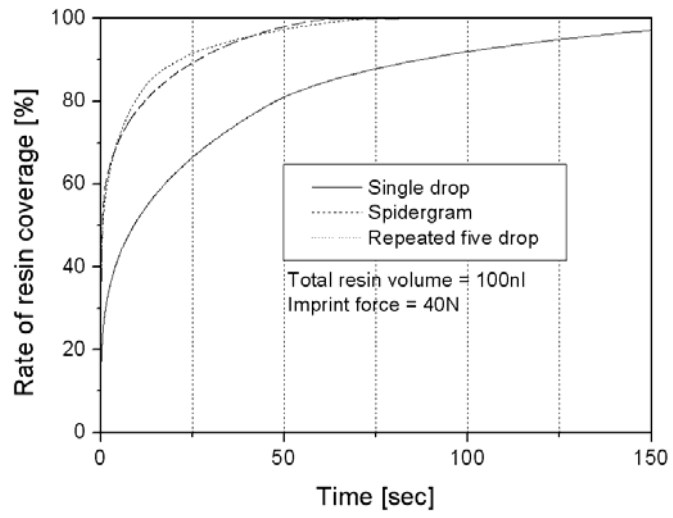
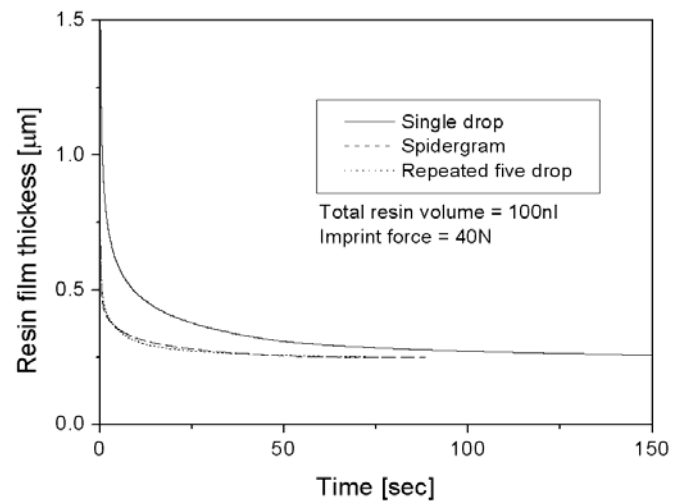


Figure 21 Resin-spreading time of the single-drop recipe with respect to the droplet volume and imprint force



(a)



(b)

Figure 22 Time evolution of (a) the resin coverage rate and (b) resin film thickness with respect to the resin dispensing recipe

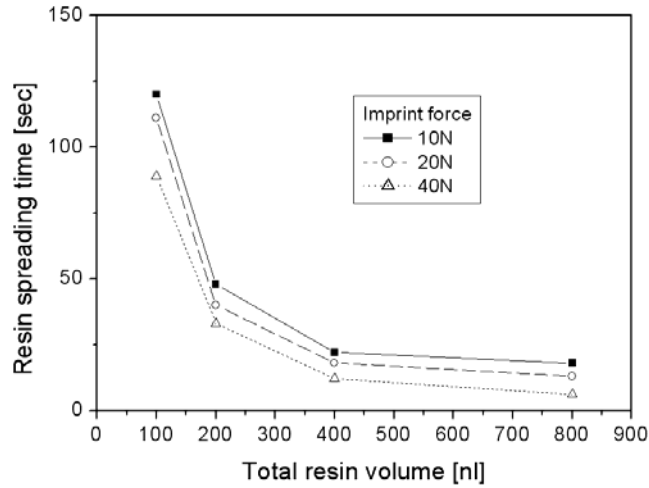


Figure 23 Resin-spreading time of the spidergram recipe for various droplet volumes and imprint forces

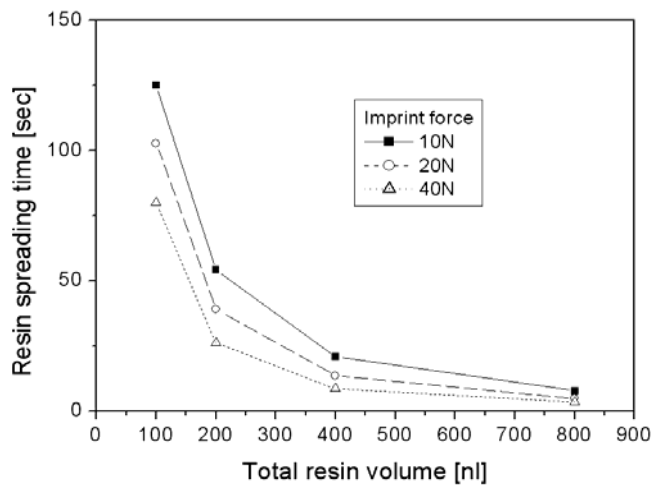


Figure 24 Resin-spreading time of the repeated five drop recipe for various droplet volumes and imprint forces

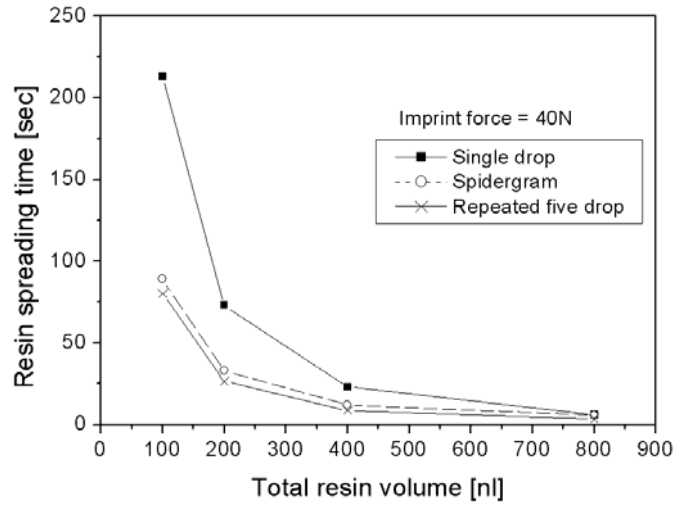


Figure 25 Comparison of resin-spreading times of the single-drop, spidergram and repeated five drop recipes

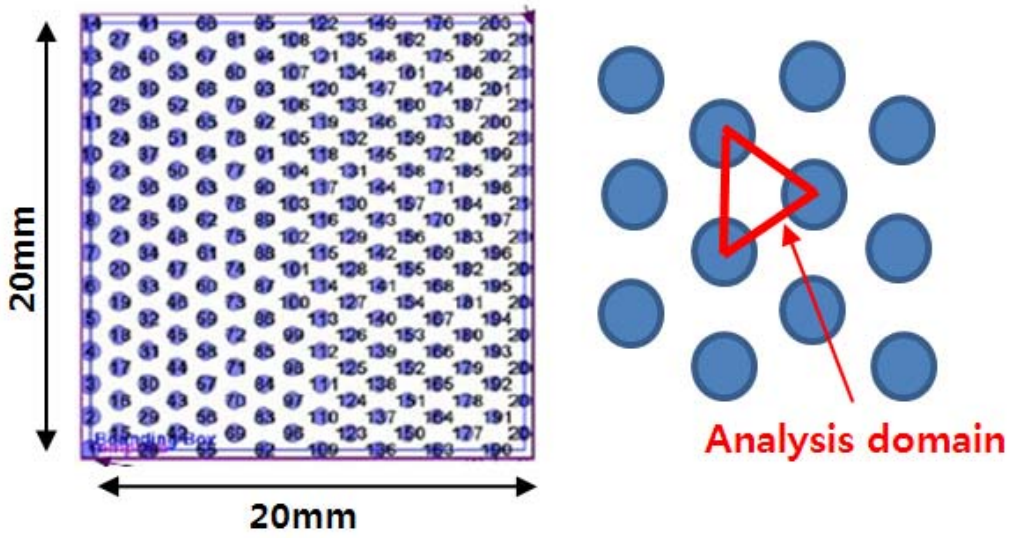


Figure 26 Analysis domain of the zigzag recipe

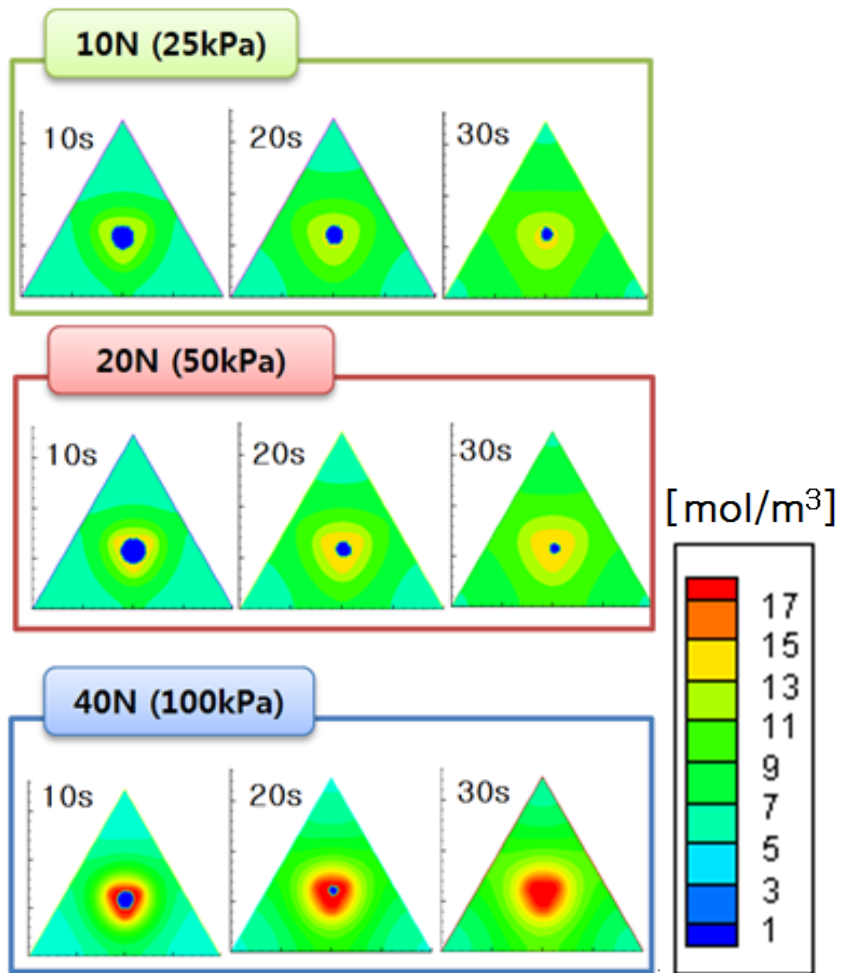


Figure 27 Entrapped gas dissolution simulation results: Gas concentration contours for different imprint forces

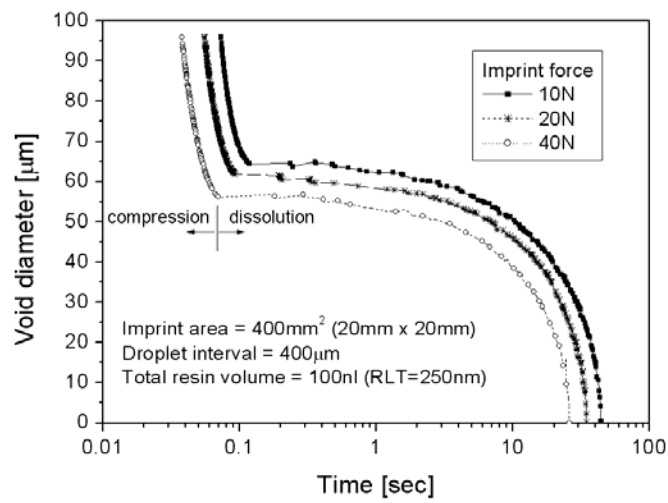


Figure 28 Time evolution of entrapped gas void diameters for imprint forces of 10N, 20N, and 40N

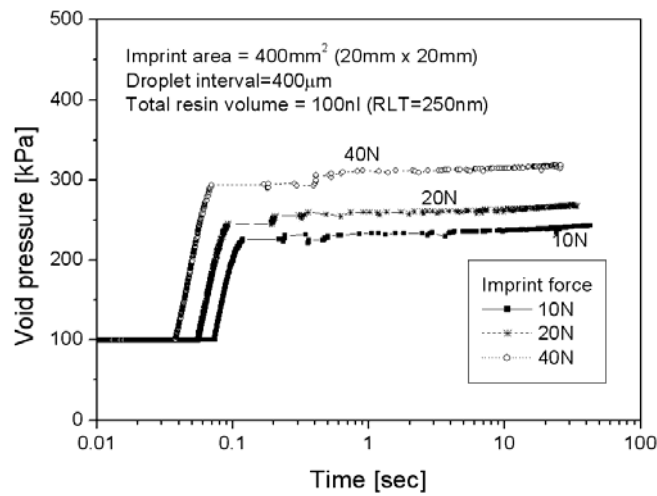


Figure 29 Time evolution of entrapped gas void pressure for imprint forces of 10N, 20N, and 40N

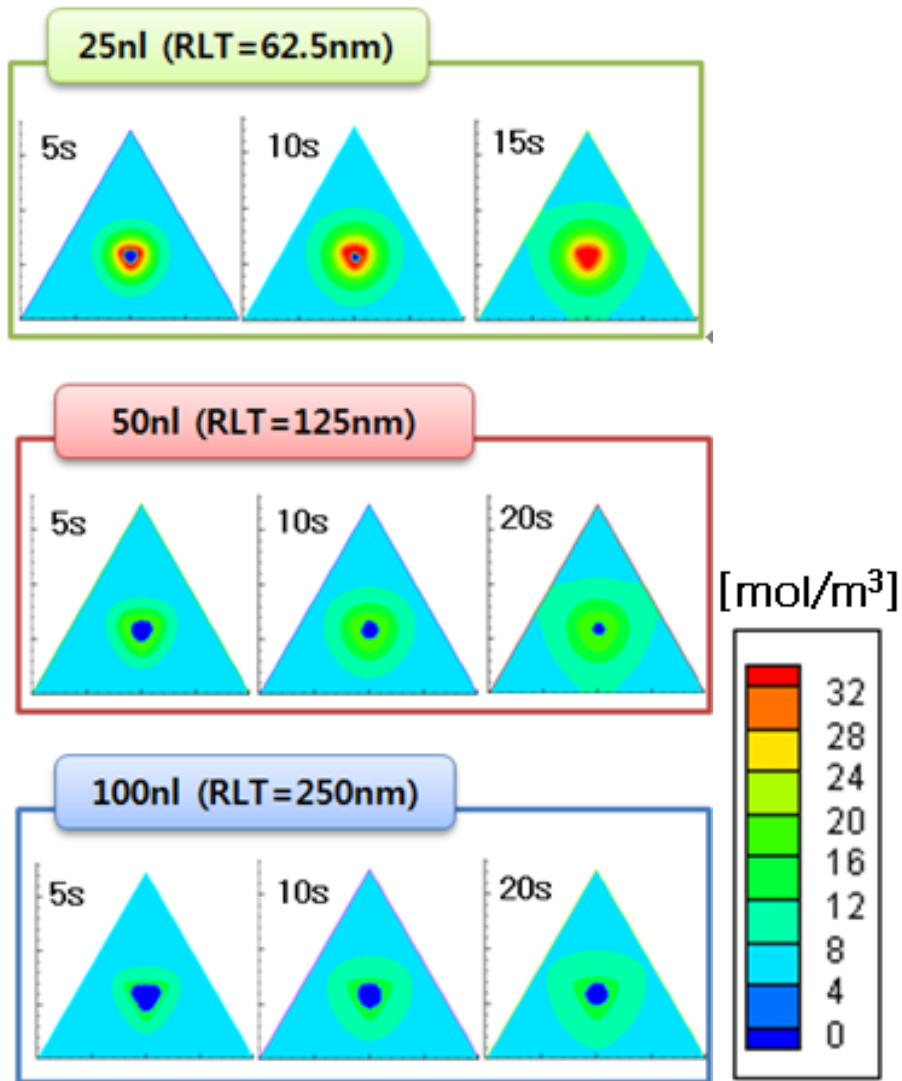


Figure 30 Entrapped gas dissolution simulation results: Gas concentration contours for different resin volumes

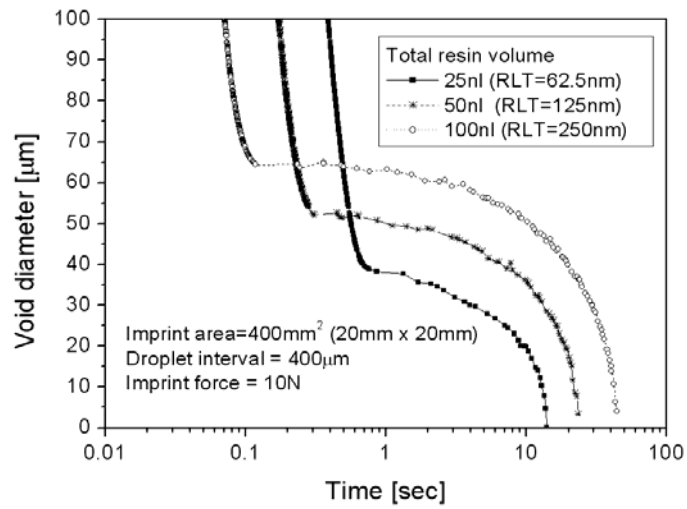


Figure 31 Time evolution of entrapped gas void diameters for total resin volumes of 25nl, 50nl, and 100nl

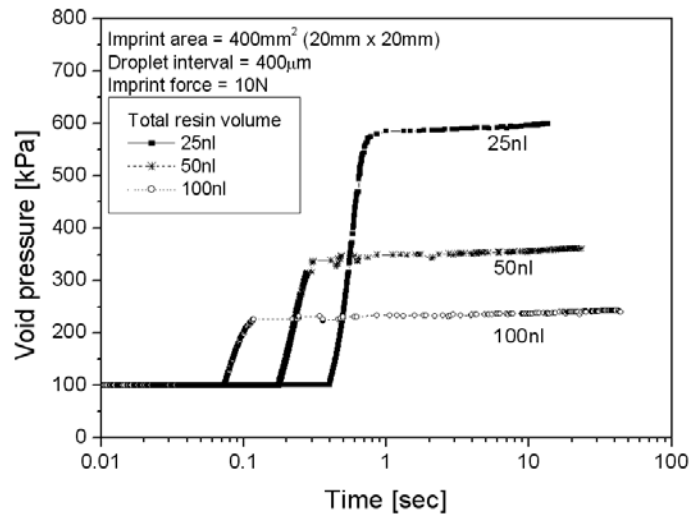
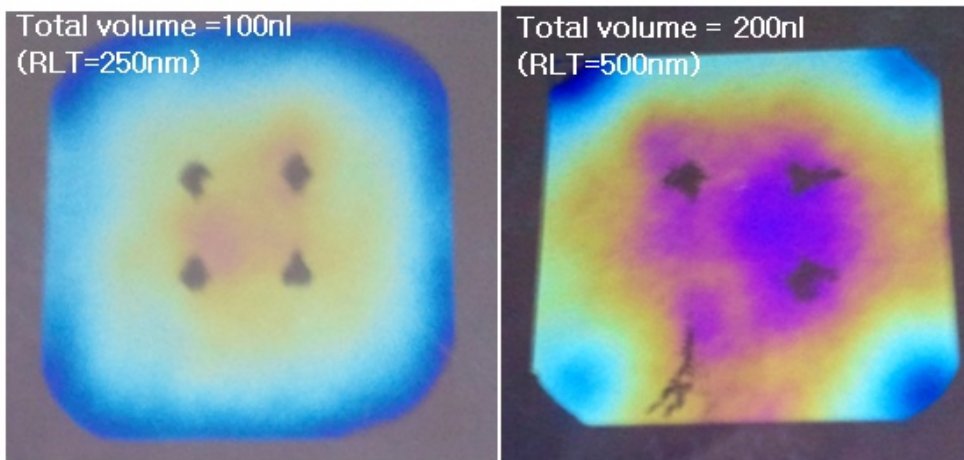
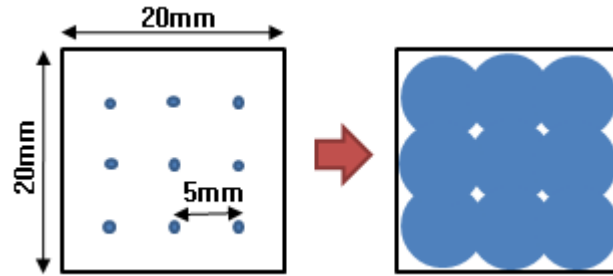


Figure 32 Time evolution of entrapped gas void pressure for total resin volumes of 25nl, 50nl, and 100nl



(a)

(b)

Figure 33 Results of gas void entrapment tests with different residual layer thicknesses: (a) RLT=250nm, (b)RLT=500nm

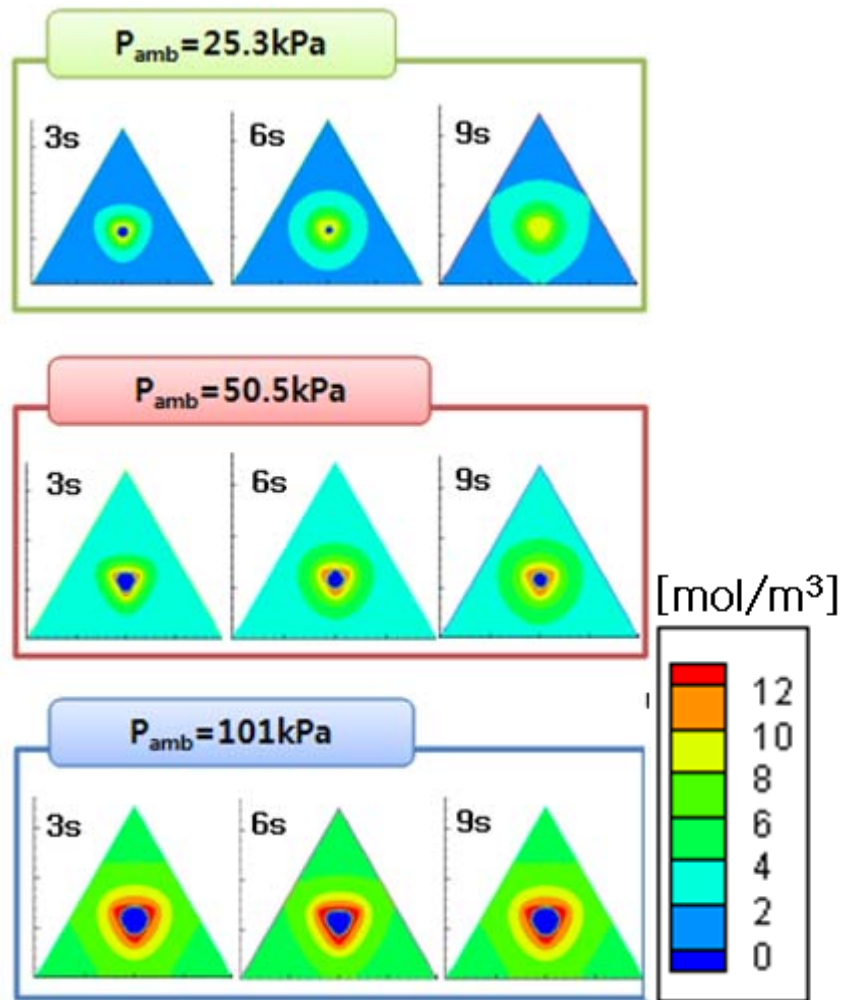


Figure 34 Entrapped gas dissolution simulation results: Gas concentration contours for ambient gas pressures

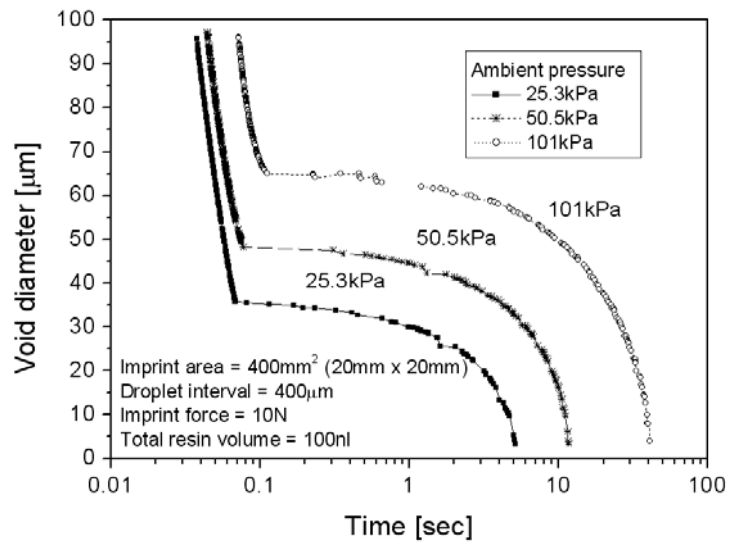


Figure 35 Time evolution of entrapped gas void diameters for imprint pressures of 25.3kPa, 50.5kPa, and 101kPa

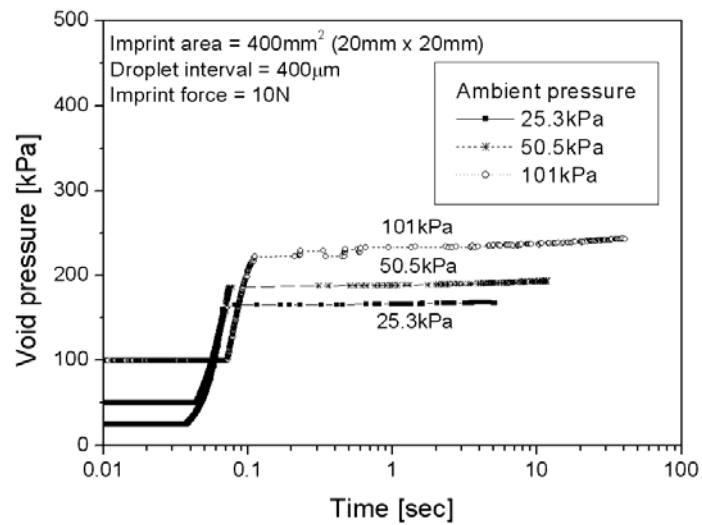


Figure 36 Time evolution of entrapped gas void pressure for imprint pressures of 25.3kPa, 50.5kPa, and 101kPa

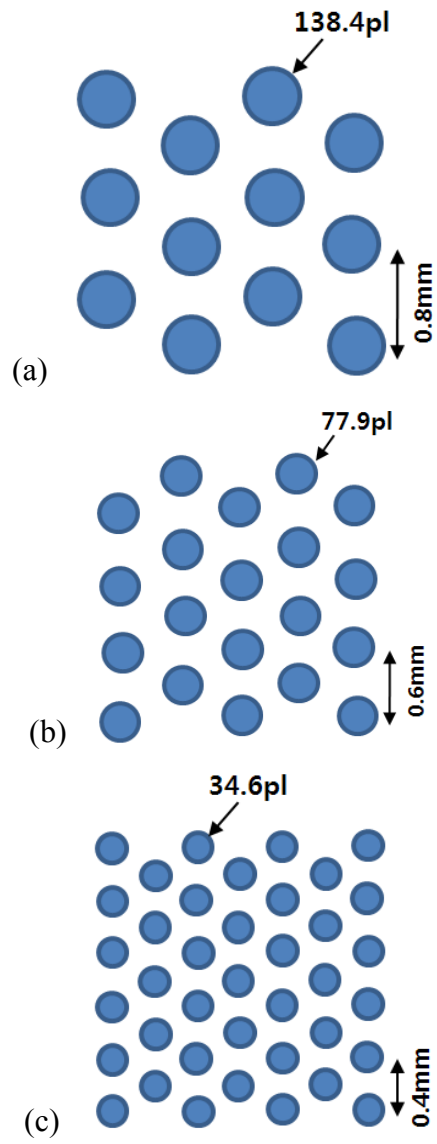


Figure 37 Zigzag recipes with different droplet volumes and intervals

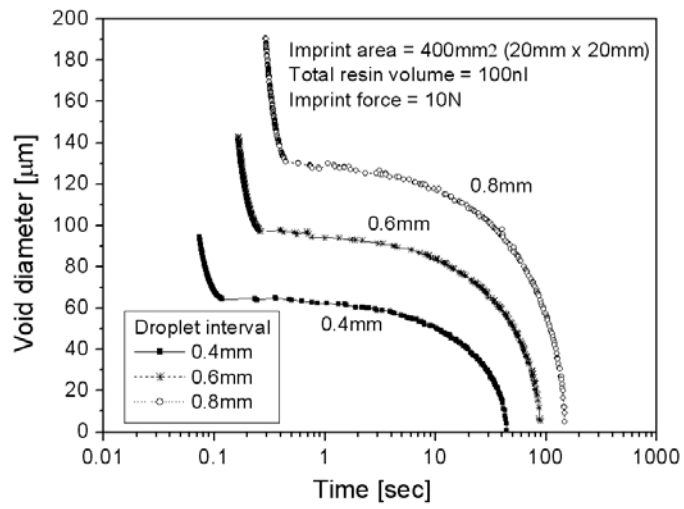


Figure 38 Time evolution of entrapped gas void diameters for dispensing intervals of 0.4mm, 0.6mm, and 0.8mm

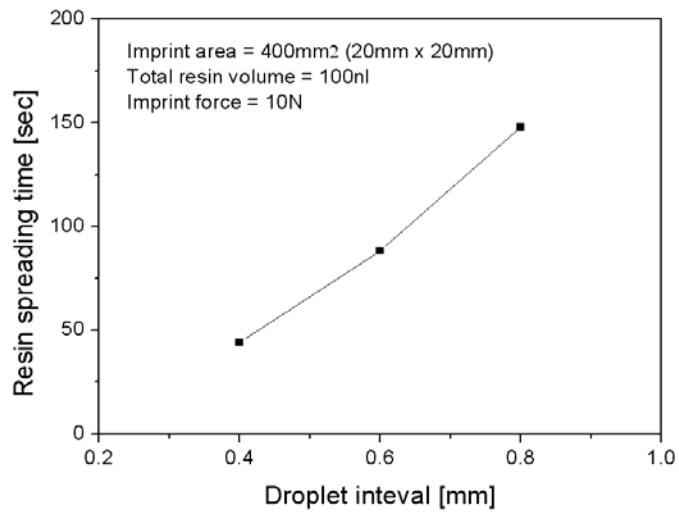


Figure 39 Resin-spreading time with respect to the droplet interval

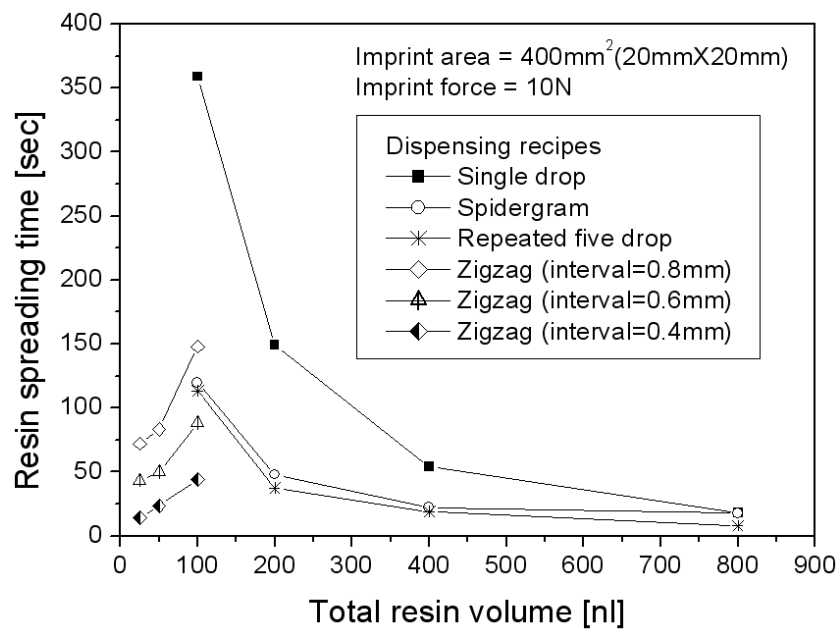


Figure 40 Comparison of resin-spreading times for various recipes

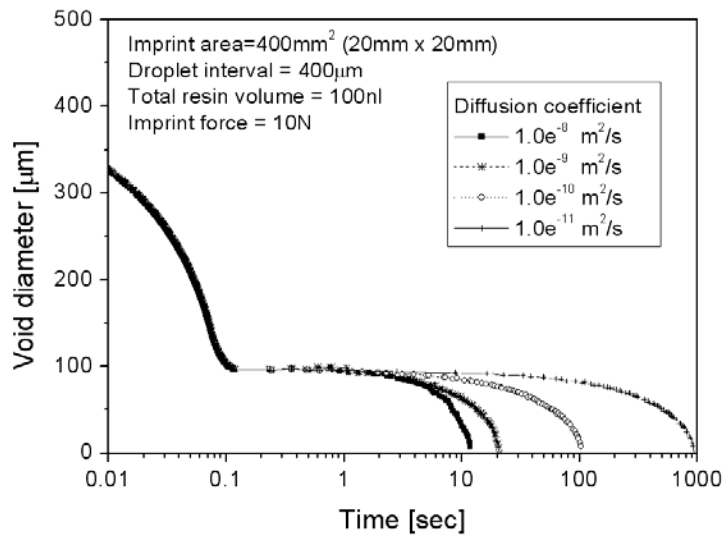


Figure 41 Time evolution of entrapped gas void diameters with respect to the diffusion coefficient

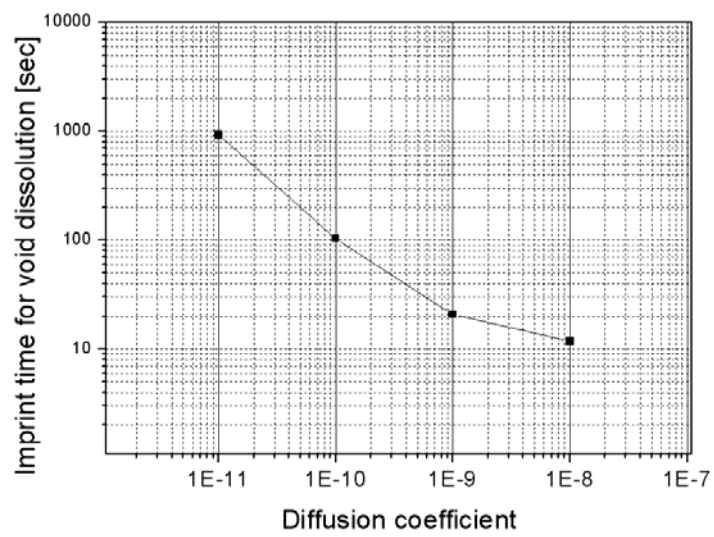


Figure 42 Resin-spreading time with respect to the diffusion coefficient

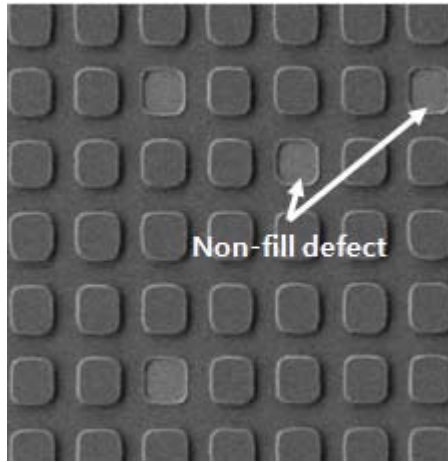


Figure 43 Example image of a non-fill defect [30]

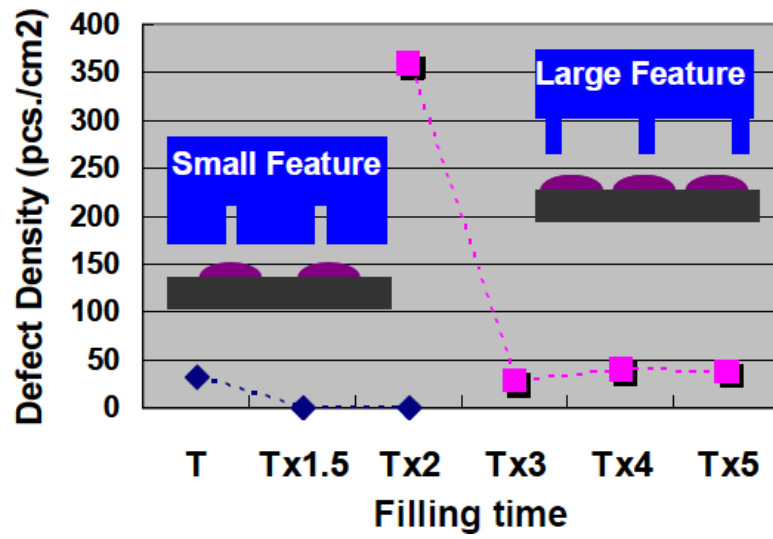


Figure 44 Relationship between the filling time and defect density of two types of patterns [30]

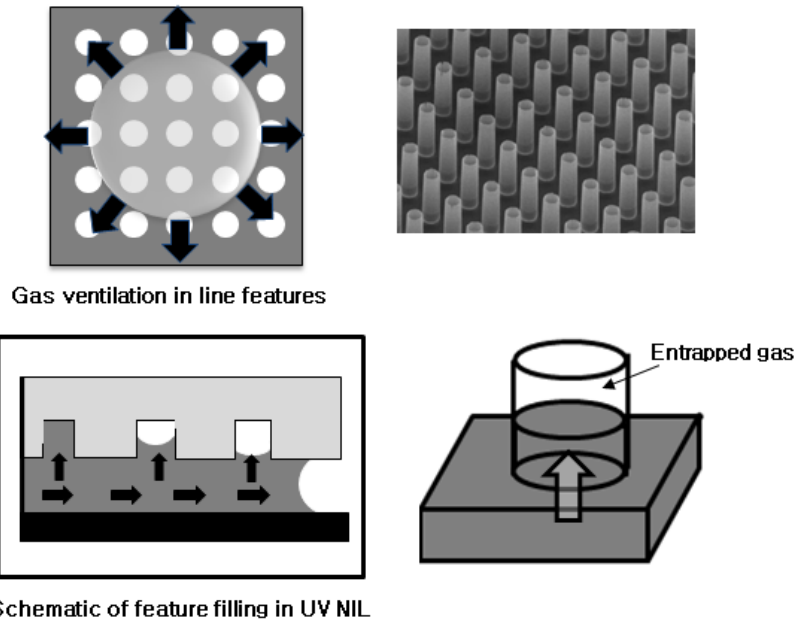


Figure 45 Schematics of resin filling into pillar cavities during the SFIL process

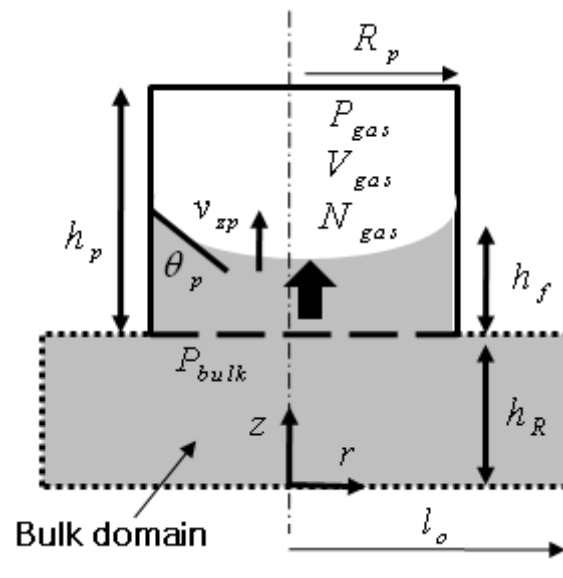


Figure 46 Resin filling and gas dissolution model for pillar patterns

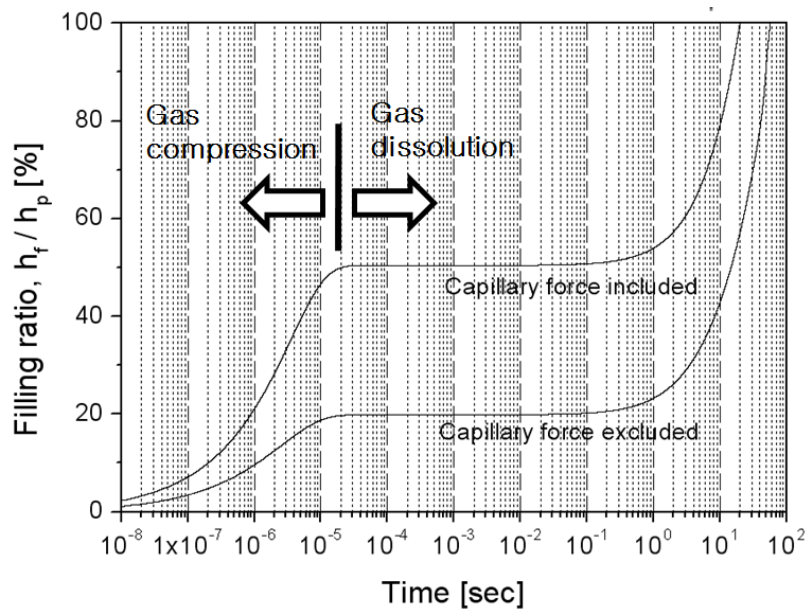


Figure 47 Time evolution of the feature-filling ratio into a pore with a 250nm radius and a 1000nm depth

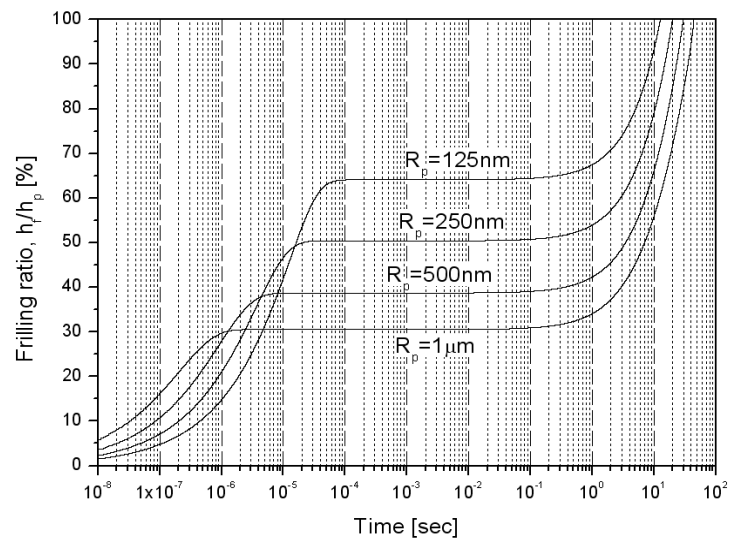


Figure 48 Time evolution of the feature-filling ratio for pores with radii of 125nm, 250nm, 500nm, and 1000nm

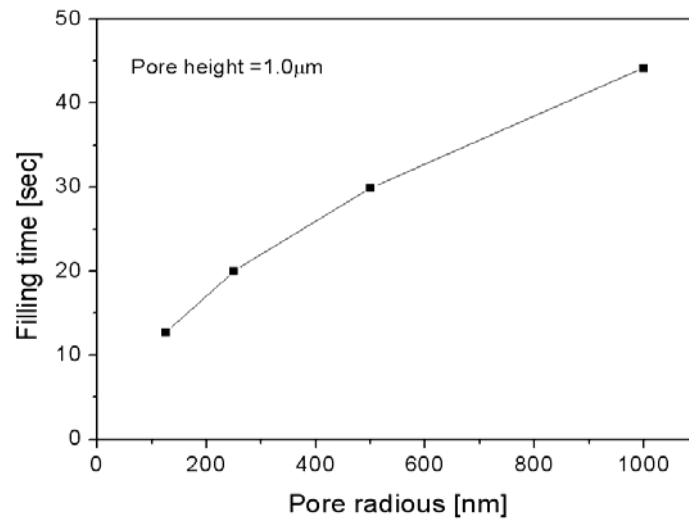


Figure 49 Resin-filling time with respect to the pore radius

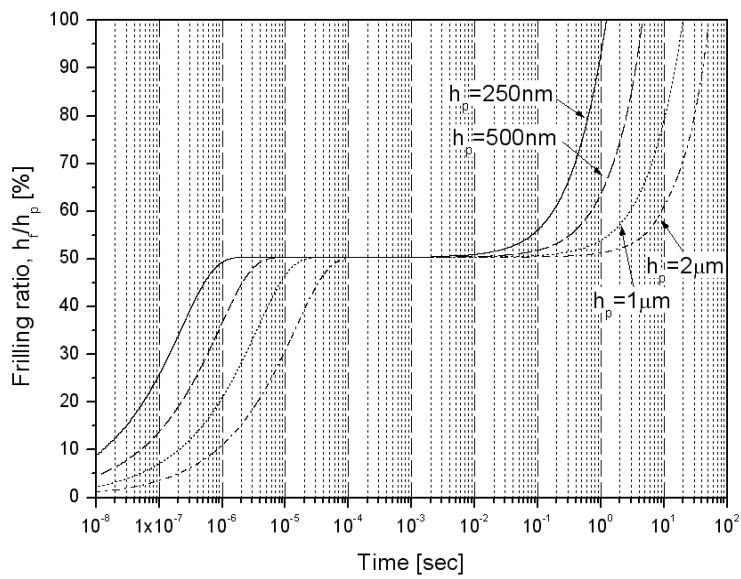


Figure 50 Time evolution of the feature-filling ratio for pores with depths of 250nm, 500nm, 1000nm, and 2000nm

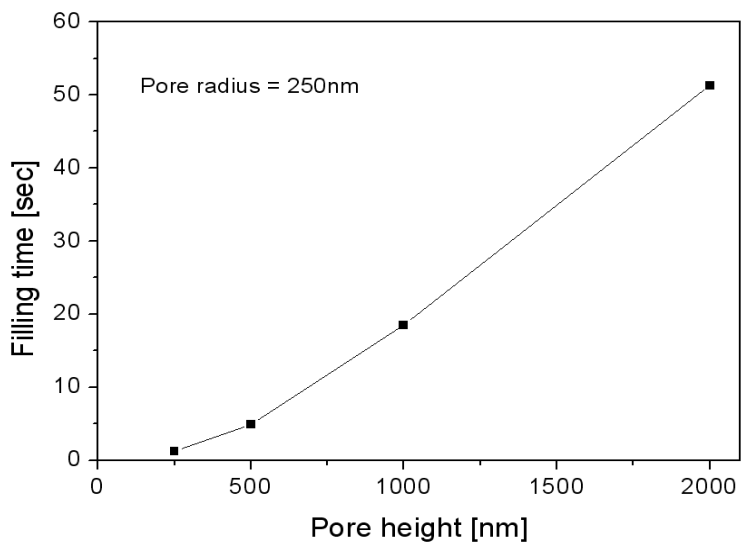


Figure 51 Resin-filling time with respect to the pore height

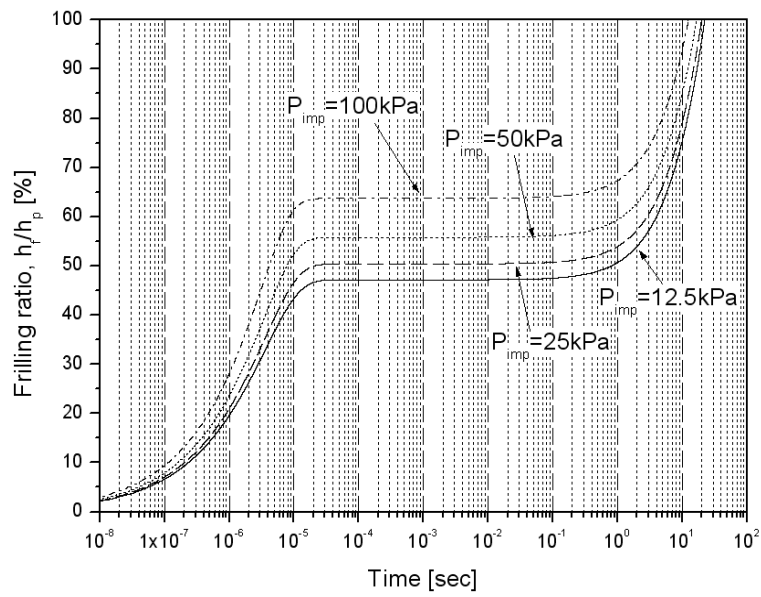


Figure 52 Time evolution of the feature-filling ratio for imprint pressures of 12.5kPa, 25kPa, 50kPa, and 100kPa

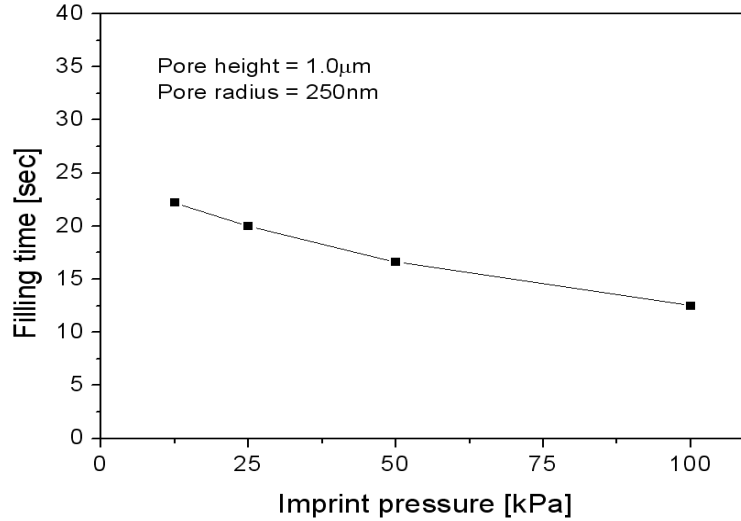


Figure 53 Resin-filling time with respect to the imprint pressure

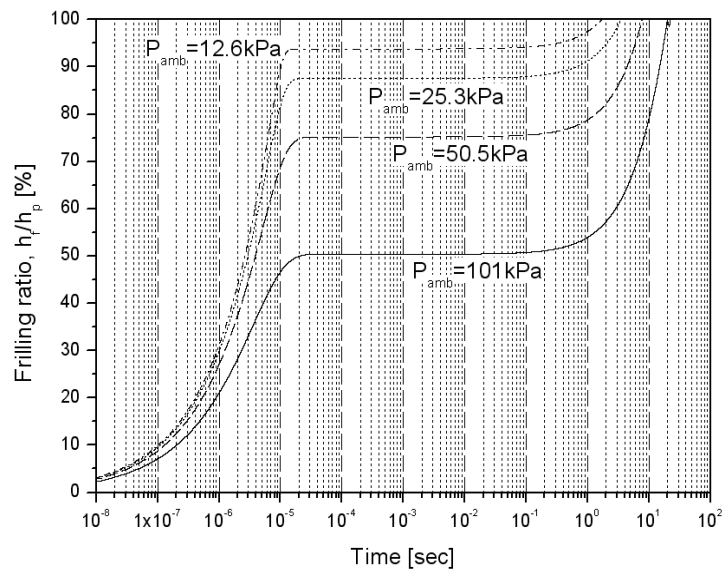


Figure 54 Time evolution of the feature-filling ratio for ambient pressures of 12.6kPa, 25.3kPa, 50.5kPa, and 101kPa

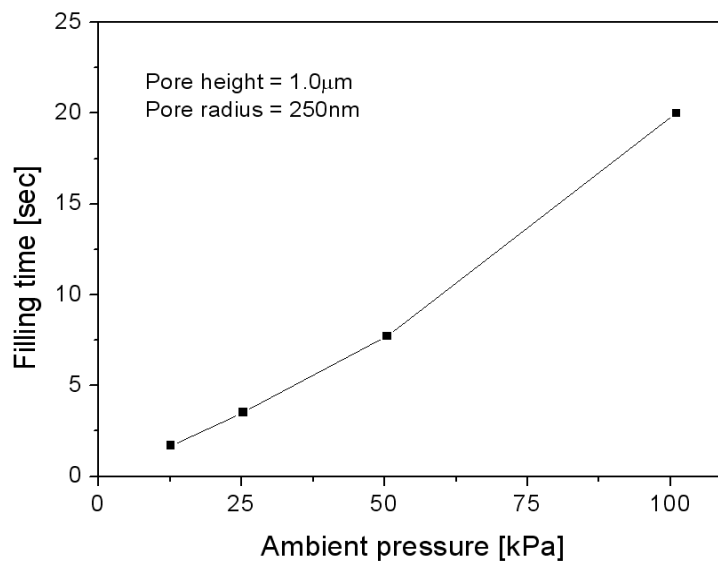
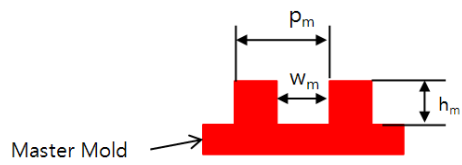
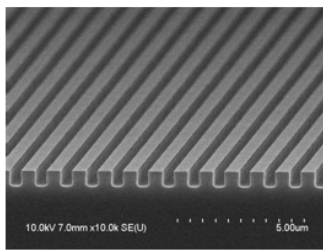


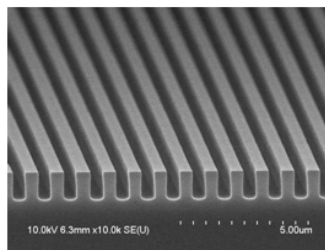
Figure 55 Resin-filling time with respect to the ambient gas pressure



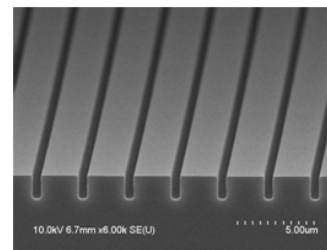
Case	w_m	P_m	h_m
A	500nm	$1\mu\text{m}$	250nm
B	500nm	$1\mu\text{m}$	500nm
C	500nm	$1\mu\text{m}$	750nm
D	500nm	$1\mu\text{m}$	$1\mu\text{m}$
E	500nm	$2\mu\text{m}$	$1\mu\text{m}$
F	500nm	$4\mu\text{m}$	$1\mu\text{m}$



Case B



Case D



Case F

Figure 56 Geometries of master molds and SEM images of the master mold cross-sections

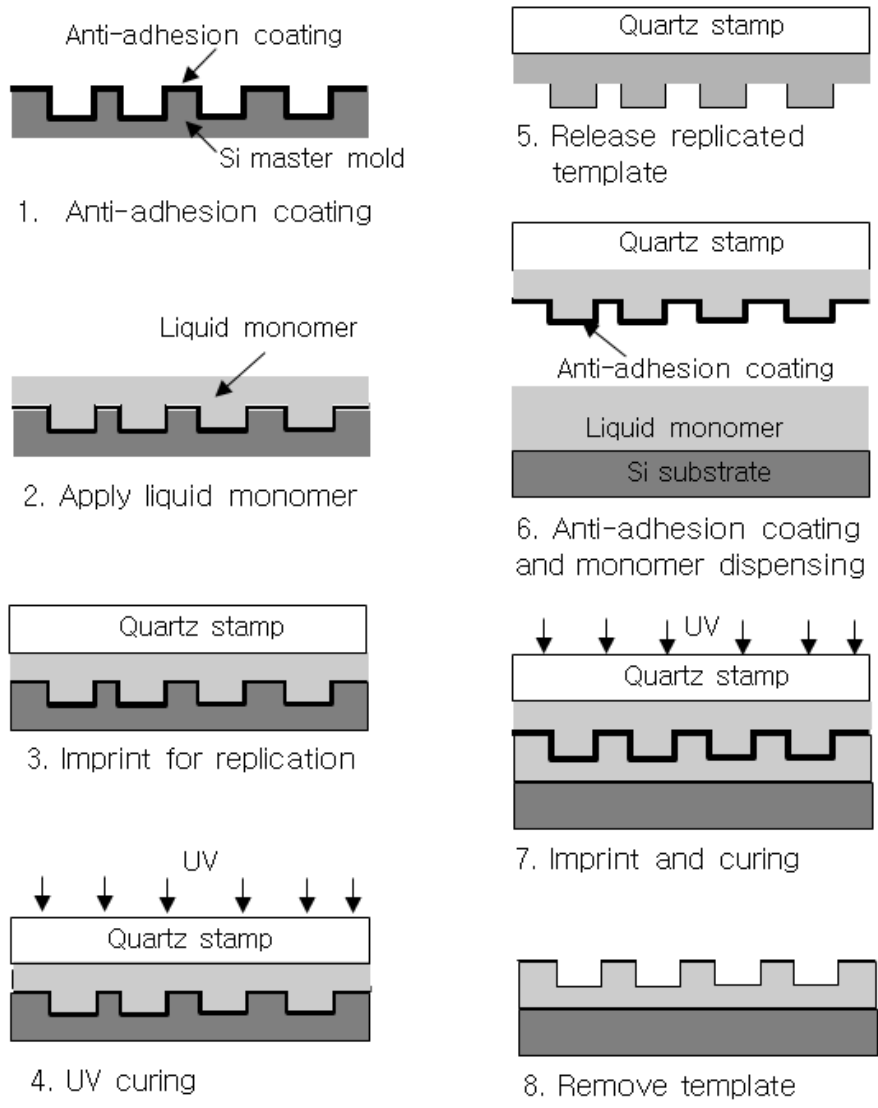
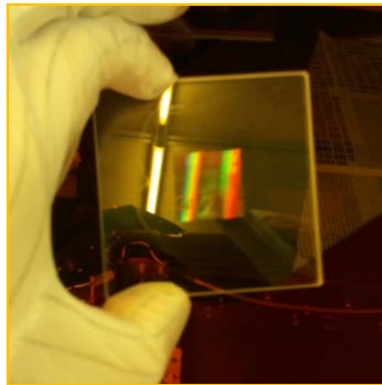


Figure 57 Procedure of soft mold replication and imprint using the SFIL process

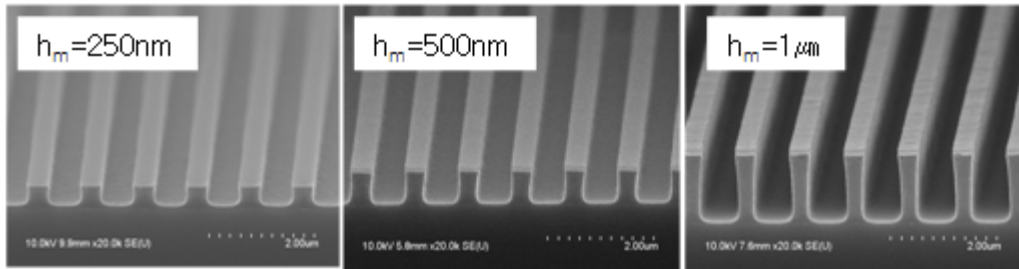


(a)

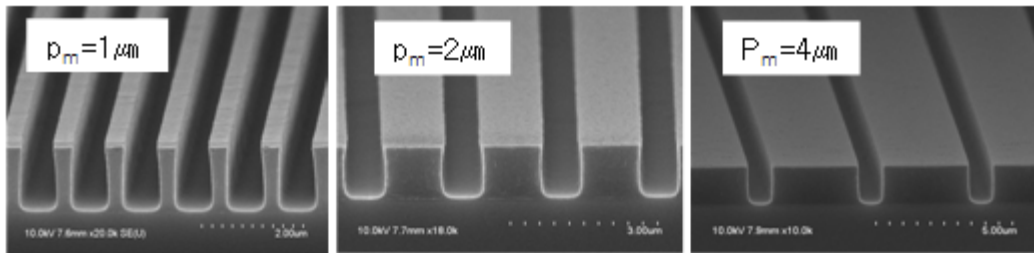


(b)

Figure 58 A quartz template: (a) before pattern replication and (b) after pattern replication



(a)



(b)

Figure 59 SEM images of cross-sections of imprinted patterns with (a) various heights and (b) various pitches

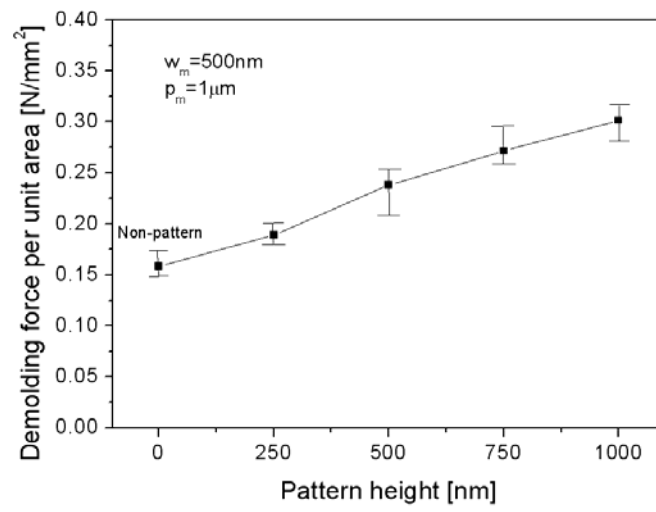


Figure 60 Demolding forces measured for various pattern heights

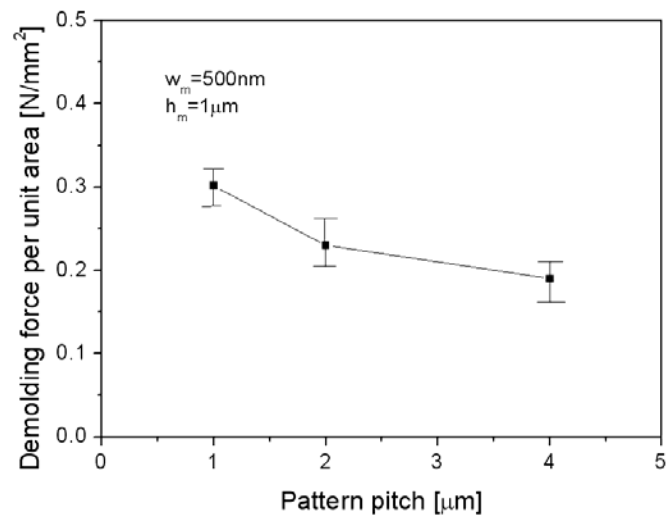


Figure 61 Demolding forces measured for various pattern pitches

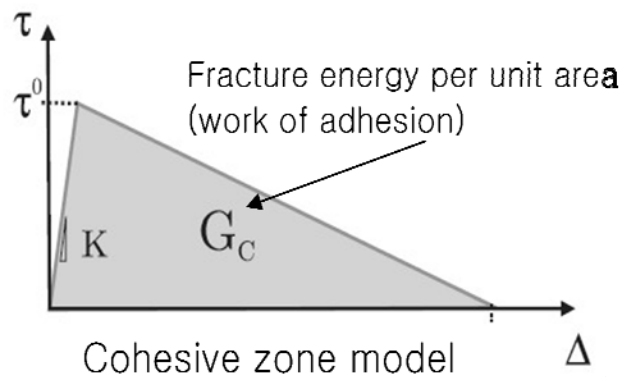


Figure 62 Conceptual figure of the cohesive zone model

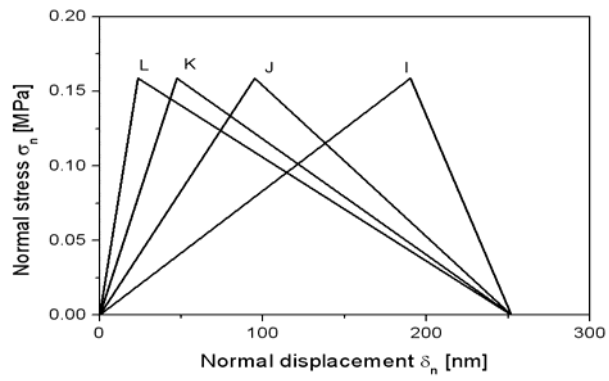
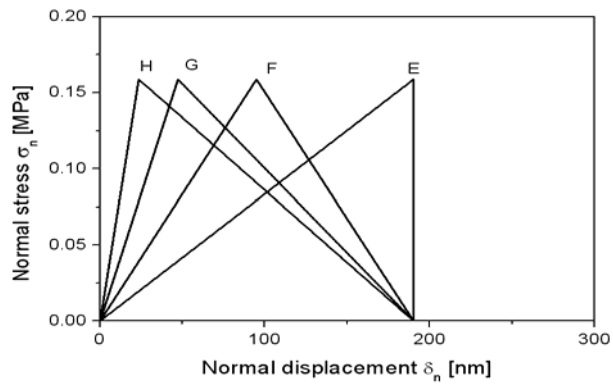
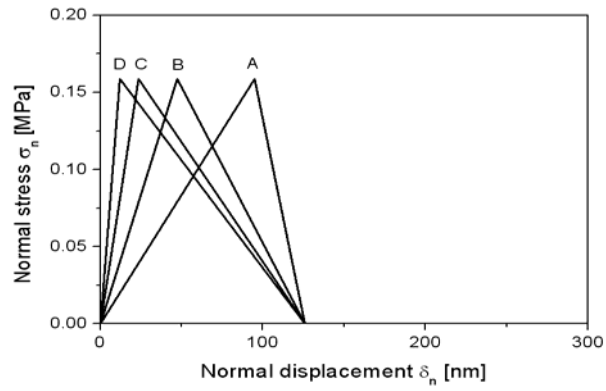


Figure 63 Cohesive zone model candidates

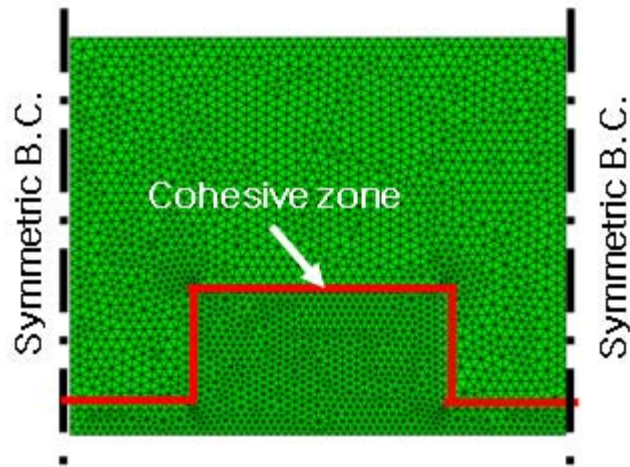


Figure 64 An example of finite element analysis model for demolding simulation.

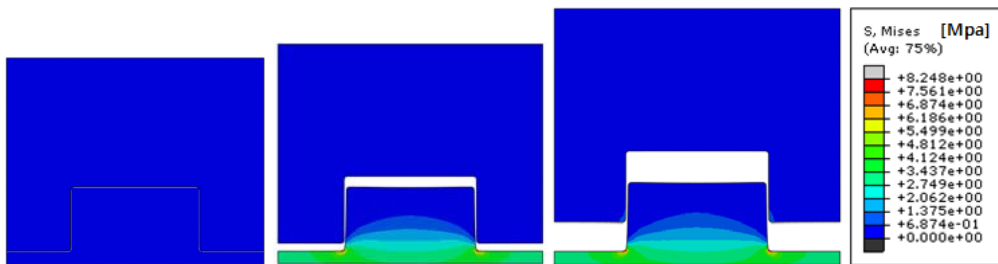


Figure 65 An example of a demolding simulation result: stress contours

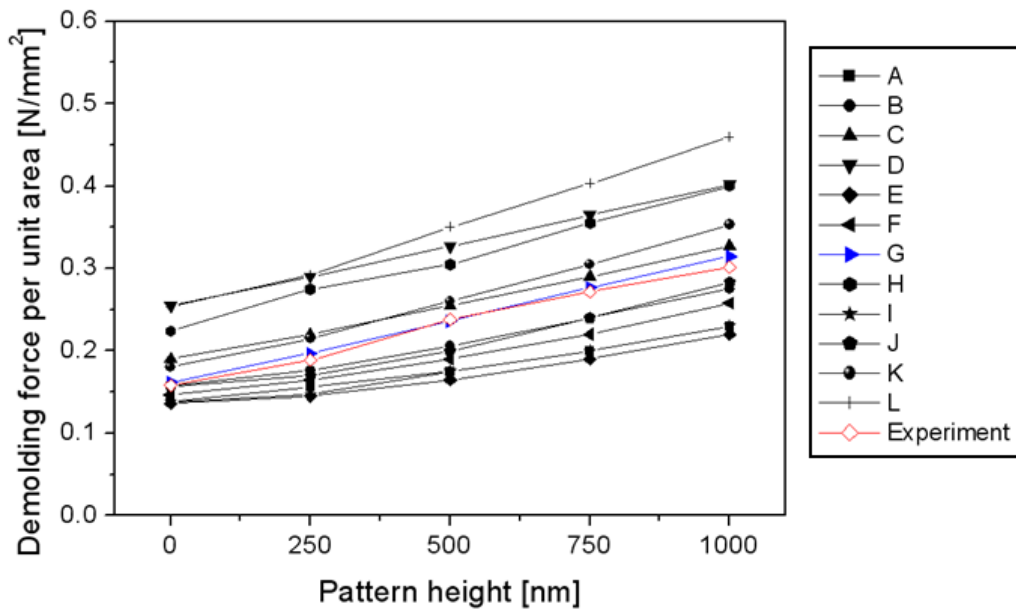


Figure 66 Comparison of experimental and numerical results with various cohesive zone models

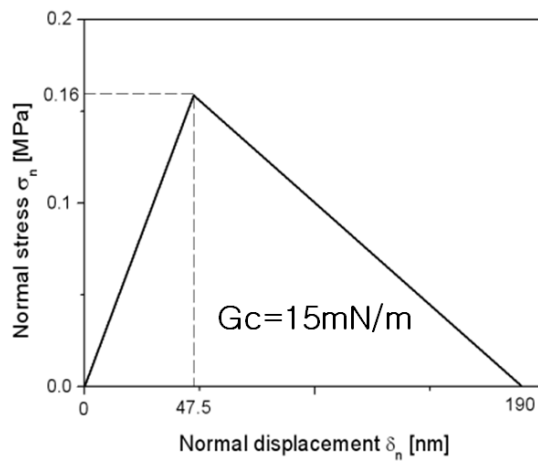


Figure 67 A cohesive zone model chosen for the demolding analyses

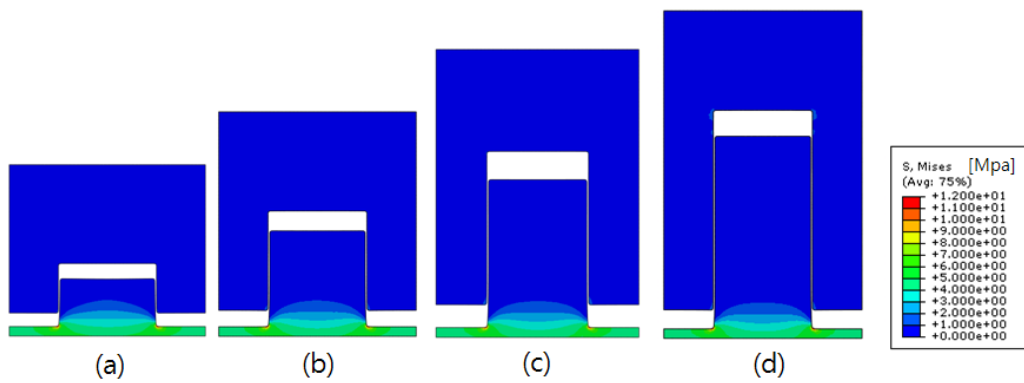


Figure 68 Stress contours obtained by demolding simulations for various pattern heights: (a) $h_m = 250\text{nm}$, (b) $h_m = 500\text{nm}$, (c) $h_m = 750\text{nm}$, and (d) $h_m = 1000\text{nm}$

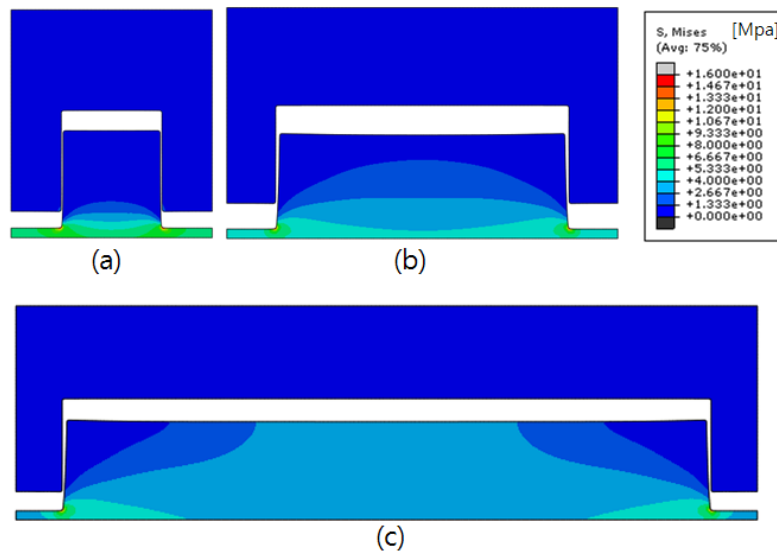


Figure 69 stress contours obtained by demolding simulations for various pattern pitches: (a) $p_m = 1\mu\text{m}$, (b) $p_m = 2\mu\text{m}$, and (c) $p_m = 4\mu\text{m}$

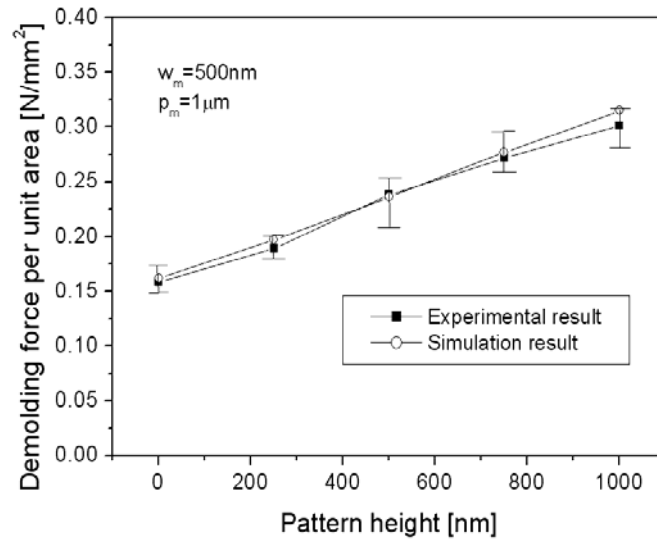


Figure 70 Maximum demolding forces with respect to the pattern height

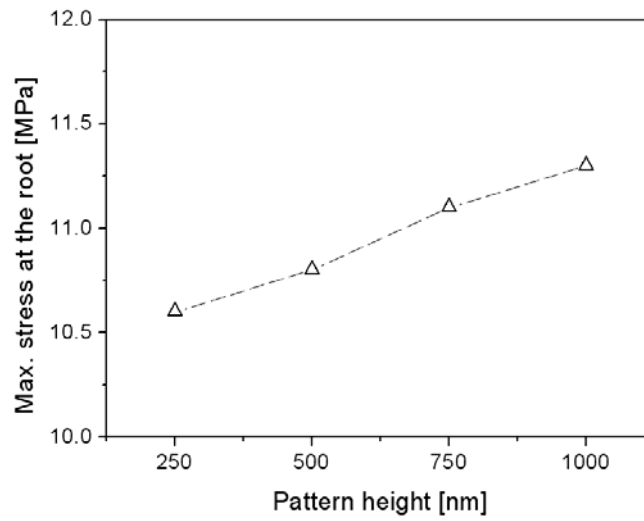


Figure 71 Maximum root stress with respect to the pattern height

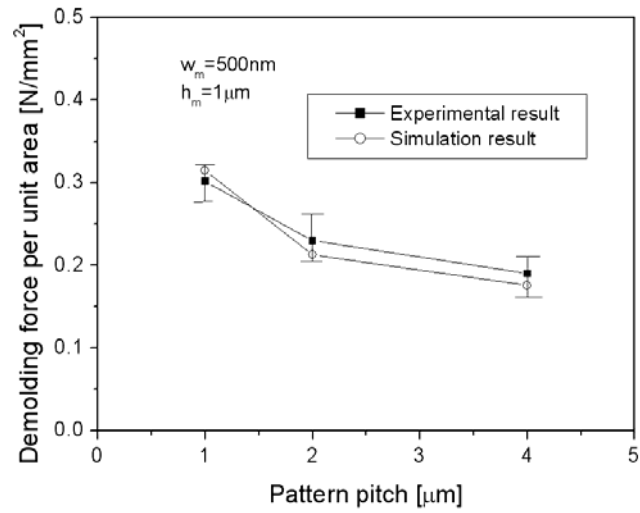


Figure 72 Maximum demolding forces with respect to the pattern pitch

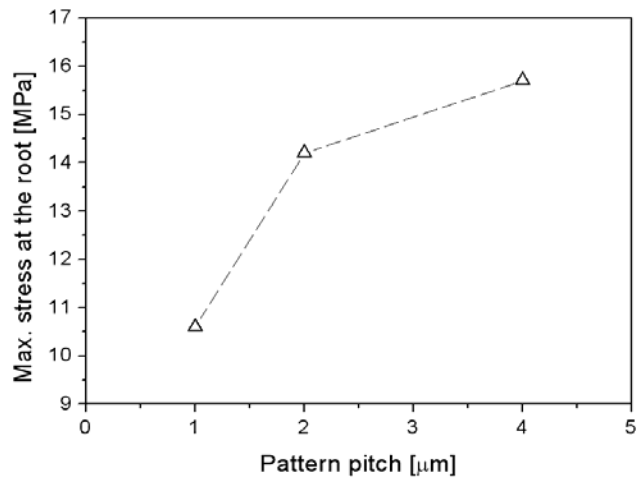


Figure 73 Maximum root stress with respect to the pattern pitch

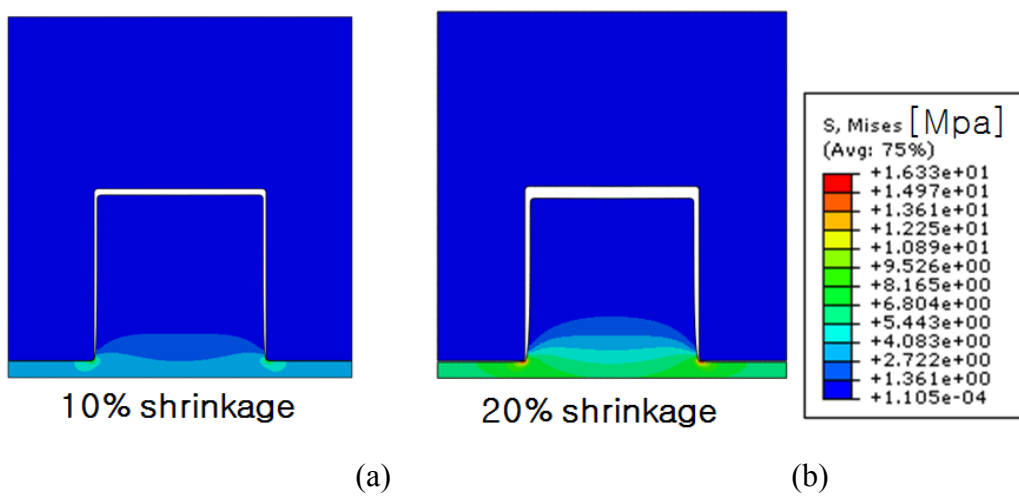
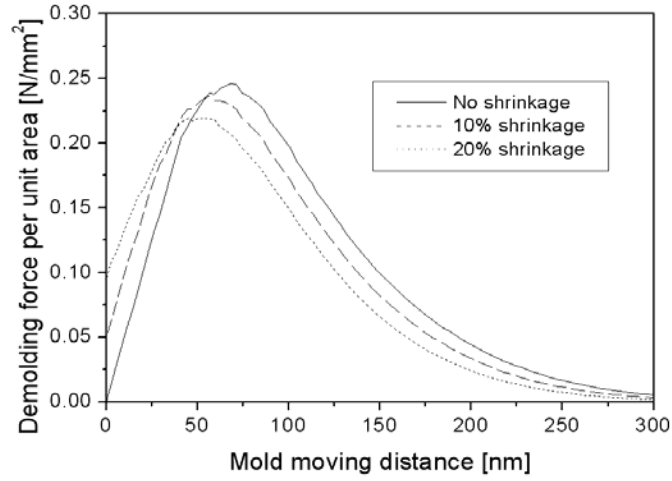
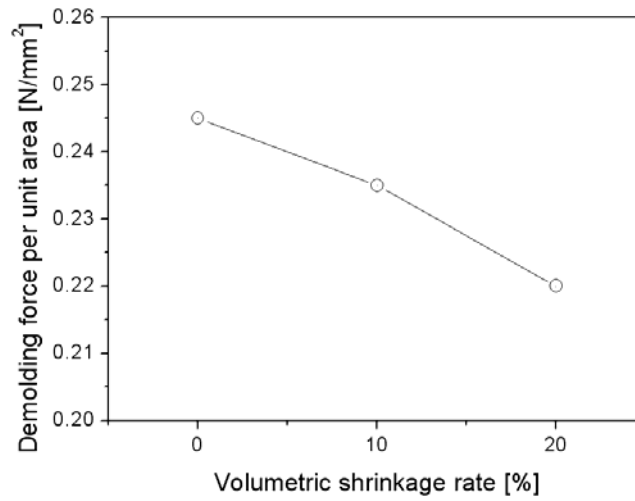


Figure 74 Stress contours and deformed shapes of a line structure after volumetric shrinkages of 10% and 20%, respectively



(a)



(b)

Figure 75 Demolding simulation results with shrinkage rates of 0%, 10%, and 20%: (a) evolution of demolding forces and (b) maximum demolding forces

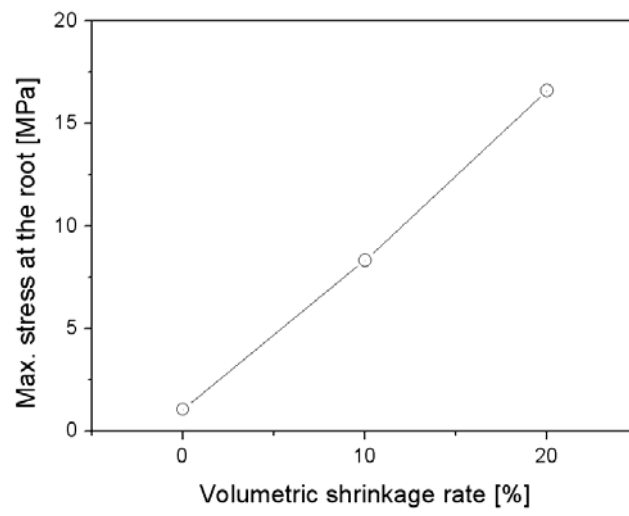


Figure 76 Maximum root stresses with respect to the shrinkage rate

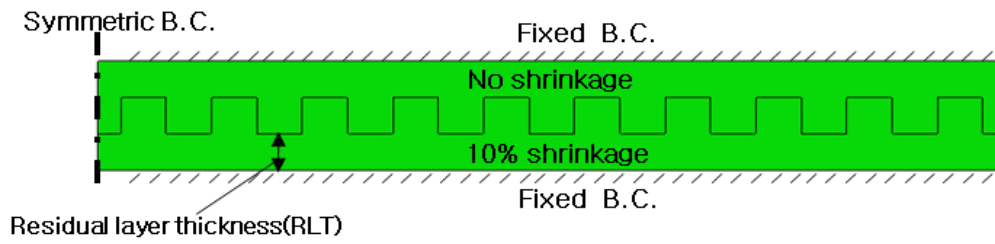


Figure 77 Simulation model to investigate the shrinkage mismatch effect in the SFIL process

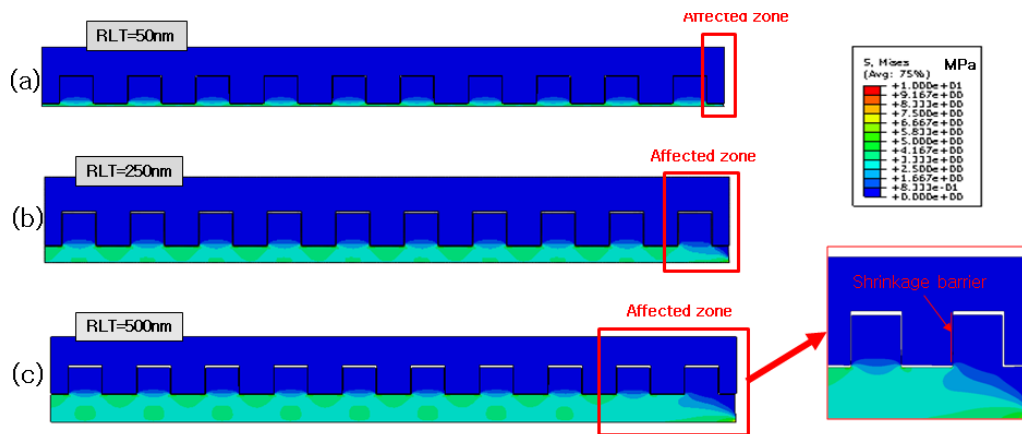
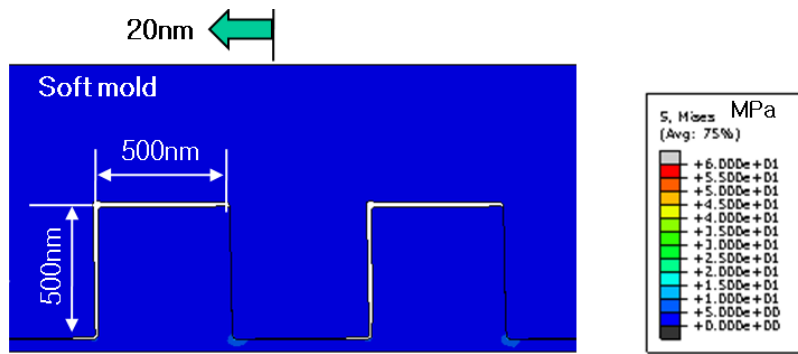
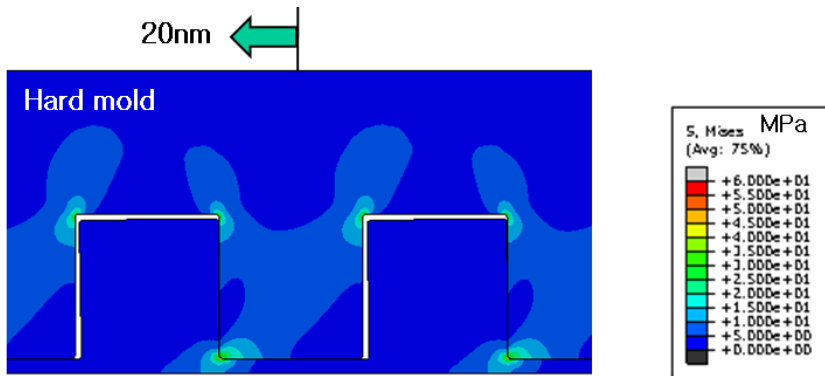


Figure 78 Effects of shrinkage mismatch in the SFIL process: simulation results with (a) RLT=50nm, (b) RLT=250nm, and (c) RLT=500nm



(a)



(b)

Figure 79 Stress contour and pattern deformation after 20nm mold shifting with a (a) soft mold and (b) hard mold

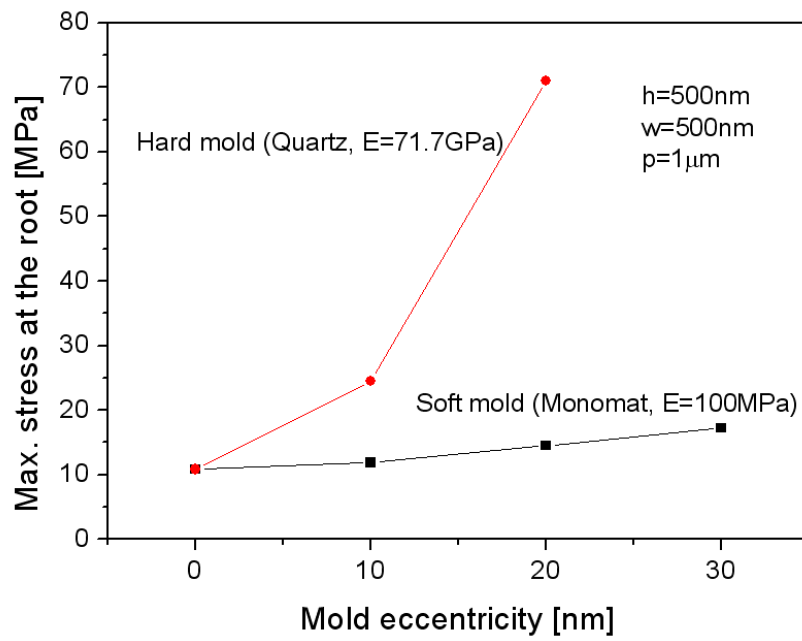


Figure 80 Maximum stress in the imprinted structure with respect to the mold eccentricity: Comparison when using a hard mold vs. a soft mold.

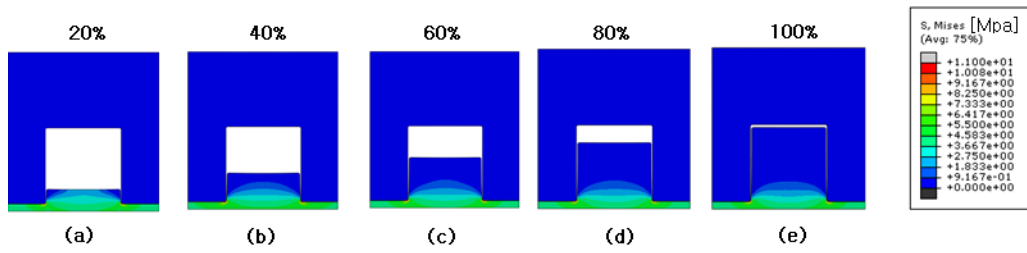


Figure 81 Demolding simulation results of partially filled line patterns with a filling ratio of (a)20%, (b)40%, (c)60%, (d)80%, and (e)100%

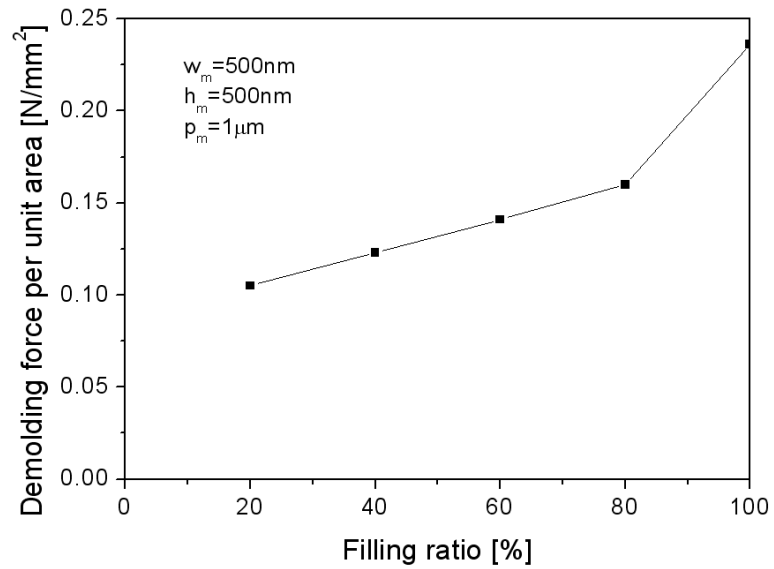


Figure 82 Demolding forces of partially filled line patterns

Tables

Table 1 Material properties and process conditions used for the single-drop spreading simulation

Parameters	Symbols	Value
Ambient pressure (MPa)	P_{amb}	0.101
viscosity (mPa s)	μ	30
surface tension (Nm ⁻¹)	γ	0.020
Contact angles	θ_1, θ_2	61 ^o , 12 ^o

Table 2 Physical parameters used for the gas dissolution simulation

Physical parameters	Value
Surface tension (N m^{-1}) ^a	0.030
Resist viscosity (mPa s) ^a	2–20
Henry's law constant ($\text{mol m}^{-3} \text{Pa}^{-1}$)	5.45×10^{-5}
Diffusion coefficient ($\text{m}^2 \text{s}^{-1}$) ^b	4.30×10^{-9}
Degree of saturation of the resist ^b	0.91
Imprint pressure (MPa) ^a	0.014–0.550
Initial resist thickness (nm) ^a	50–500
Initial resist film radius (mm) ^a	10–20
Initial bubble diameter (μm) ^a	20–800
Ambient pressure (Pa) ^a	1.01×10^5
Pressure inside the bubble (Pa)	
Shrinking rate of the bubble radius ($\mu\text{m s}^{-1}$)	
Contact angles ^a	45° , 30°

Table 3 Process parameters used for the feature-filling analysis

Parameters	Symbols	Value
Ambient pressure (MPa)	P_{amb}	0.101
viscosity (mPa s)	μ	30
surface tension (Nm ⁻¹)	γ	0.020
Contact angle	θ_p	61 ^o
Imprint pressure (MPa)	P_{imp}	0.025
Henry's law constant (mol m ³ /Pa)	C_h	5.45x10 ⁻⁵
Diffusion coefficient (m ² /s)	D	2.87x10 ⁻¹⁰
Pore radius (nm)	R_p	250
Pore height (μm)	h_p	1.0
Residual layer thickness (μm)	h_R	2.0
Bulk domain radius (μm)	l_0	10

UV 나노임프린트 리소그래피 공정에서의 수지 유동과 이형 과정에 대한 수치해석

서울대학교 대학원
기계항공공학부
손기주

요약(국문초록)

나노임프린트 리소그래피(Nanoimprint Lithography, NIL) 공정은 나노 스케일의 미세패턴을 저비용으로 대량 생산할 수 있는 기술이다. NIL 공정에서는 기판위에 수지를 도포한 후 패턴이 새겨진 몰드가 수지를 눌러, 몰드위의 패턴을 수지 위로 전사시킨다. NIL 공정은 사용되는 수지의 종류에 따라 열가소성 수지를 사용하는 Thermal NIL과 UV경화성 수지를 사용하는 UV NIL로 구분된다. UV 경화성 수지의 경우 점도가 낮고 경화 속도가 빠르기 때문에 고해상도 패턴의 대량 생산하기에는 UV NIL이 보다 적합하다.

본 연구는 UV NIL 공정 중 하나인 Step and Flash Imprint Lithography(SFIL) 공정에서의 수지 유동과 이형 특성을 다룬다. SFIL 공정에서의 수지 유동을 분석하기 위하여 수치해석 프로그램을 개발하였다.

다양한 수지 액적의 배치 방법에 따른 수지 퍼짐 시간을 잔류층 두께를 고려하여 분석하였다.

액상 수지가 패턴 내부로 충전되는 과정 또한 수치해석을 통하여 분석하였다. 모세관 현상과, 패턴 내부에 갇힌 기체의 용해과정을 고려하였으며, 패턴의 크기, 임프린트 압력, 진공도 등의 영향을 살펴 보았다.

마지막으로, 몰드가 이형되는 과정에서 발생하는 이형력과 응력 분포 등을 유한요소 해석을 통해 분석하였다. 몰드와 수지간의 부착력을 구현하기 위하여 몰드와 수지의 경계면에 Cohesive zone model을 적용하였다. 패턴의 형상, 경화과정에서의 수지의 수축률 등이 이형과정에 미치는 영향을 정량적으로 분석하였다.

본 연구에서 개발 된 수치해석 기법들을 이용하여 SFIL 공정에서의 주요 공정들을 모사할 수 있으며, 이를 이용하여 SFIL 공정에서의 제품 품질 향상과 함께 공정의 최적화를 통한 설계 및 생산 비용을 절감에 기여할 수 있을 것으로 기대된다.

주요어 : 나노임프린트 리소그래피, 수지 유동, 모세관 현상, 기포 용해, 이형, Volume of Fluid(VOF), Cohesive zone model(CZM)

학번 : 2010 - 30793